2015-12

Design and analysis of side-looking sonar experiments

Tsaprazis, Konstantinos

Monterey California. Naval Postgraduate School

NAVAL POSTGRADUATE SCHOOL

MONTEREY, CALIFORNIA

THESIS

DESIGN AND ANALYSIS OF SIDE-LOOKING-SONAR EXPERIMENTS

by

Konstantinos Tsaprazis

December 2006

Thesis Advisor:	Lawrence J. Ziomek
Thesis Co-advisor:	Bruce Denardo

Approved for public release; distribution is unlimited

THIS PAGE INTENTIONALLY LEFT BLANK

REPORT DOCUMENTATION PAGE			*Form Approved OMB No. 0704-0188*
Public reporting burden for this collection of information is estimated to average 1 hour per response, including the time for reviewing instruction, searching existing data sources, gathering and maintaining the data needed, and completing and reviewing the collection of information. Send comments regarding this burden estimate or any other aspect of this collection of information, including suggestions for reducing this burden, to Washington headquarters Services, Directorate for Information Operations and Reports, 1215 Jefferson Davis Highway, Suite 1204, Arlington, VA 22202-4302, and to the Office of Management and Budget, Paperwork Reduction Project (0704-0188) Washington DC 20503.			
1. AGENCY USE ONLY *(Leave blank)*	**2. REPORT DATE** December 2006	**3. REPORT TYPE AND DATES COVERED** Master's Thesis	
4. TITLE AND SUBTITLE: Design and Analysis of Side-Looking Sonar Experiments			**5. FUNDING NUMBERS**
6. AUTHOR(S) Konstantinos Tsaprazis			
7. PERFORMING ORGANIZATION NAME(S) AND ADDRESS(ES) Naval Postgraduate School Monterey, CA 93943-5000			**8. PERFORMING ORGANIZATION REPORT NUMBER**
9. SPONSORING /MONITORING AGENCY NAME(S) AND ADDRESS(ES) N/A			**10. SPONSORING/MONITORING AGENCY REPORT NUMBER**
11. SUPPLEMENTARY NOTES The views expressed in this thesis are those of the author and do not reflect the official policy or position of the Department of Defense or the U.S. Government.			
12a. DISTRIBUTION / AVAILABILITY STATEMENT Approved for public release; distribution is unlimited			**12b. DISTRIBUTION CODE**

13. ABSTRACT (maximum 200 words)

This research concerns the design and analysis of different Side-Looking Sonar experiments in order to satisfy different operational requirements. The different designs and analysis have been done via computer simulation. Side-Looking Sonar (also known as side-scan sonar) is known for very high quality, high resolution, ocean bottom imaging. Hence, it is used for bathymetric surveys commonly called seafloor mapping. It is able to rapidly survey large ocean areas for bottom and suspended sea-mines or other kinds of threats. Another operational aspect of these systems is that they allow autonomous underwater vehicles (AUVs) to conduct operations, mostly in shallow water and near land. Thus, Side-Looking Sonar can be a very useful device in littoral warfare operations. This research has defined the basic parameters that rule the operation of a Side-Looking Sonar and, furthermore, analyzed various aspects that affect the performance of these parameters. Special focus was given to the various operational requirements and conditions that a designer or a user may encounter in realistic situations. Towards that end, many numerical examples are presented. Moreover, this research has tried to indicate the various problems that may arise when a Side-Looking Sonar operates in its near-field region and suggests certain solutions. The active sonar equation and its factors were explained and were evaluated for a realistic example of mine detection as well.

14. SUBJECT TERMS			**15. NUMBER OF PAGES**
Side-Looking Sonar, Side-scan sonar, ocean bottom imaging			129
			16. PRICE CODE
17. SECURITY CLASSIFICATION OF REPORT	**18. SECURITY CLASSIFICATION OF THIS PAGE**	**19. SECURITY CLASSIFICATION OF ABSTRACT**	**20. LIMITATION OF ABSTRACT**
Unclassified	Unclassified	Unclassified	UL

NSN 7540-01-280-5500

Standard Form 298 (Rev. 2-89)
Prescribed by ANSI Std. 239-18

THIS PAGE INTENTIONALLY LEFT BLANK

Approved for public release, distribution is unlimited

DESIGN AND ANALYSIS OF SIDE-LOOKING SONAR EXPERIMENTS

Konstantinos Tsaprazis
Lieutenant Junior Grade, Hellenic Navy
B.S., Hellenic Naval Academy, 1998

Submitted in partial fulfillment of the
requirements for the degree of

MASTER OF SCIENCE IN APPLIED PHYSICS
AND
MASTER OF SCIENCE IN SYSTEMS ENGINEERING

from the

NAVAL POSTGRADUATE SCHOOL
December 2006

Author: Konstantinos Tsaprazis

Approved by: Lawrence J. Ziomek
Thesis Advisor

Bruce Denardo
Thesis Co-Advisor

James Luscombe
Chairman, Department of Physics

Dan C. Boger
Chairman, Department of Information Sciences

THIS PAGE INTENTIONALLY LEFT BLANK

ABSTRACT

This research concerns the design and analysis of different Side-Looking Sonar experiments in order to satisfy different operational requirements. The different designs and analysis have been done via computer simulation. Side-Looking Sonar (also known as side-scan sonar) is known for very high quality, high resolution, ocean bottom imaging. Hence, it is used for bathymetric surveys, commonly called seafloor mapping. It is able to rapidly survey large ocean areas for bottom and suspended sea-mines or other kinds of threats. Another operational aspect of these systems is that they allow autonomous underwater vehicles (AUVs) to conduct operations, mostly in shallow water and near land. Thus Side-Looking Sonar can be a very useful device in littoral warfare operations. This research has defined the basic parameters that rule the operation of a Side-Looking Sonar and, furthermore, analyzed various aspects that affect the performance of these parameters. Special focus was given to the various operational requirements and conditions that a designer or a user may encounter in realistic situations. Toward that end, many numerical examples are presented. Moreover, this research has tried to indicate the various problems that may arise when a Side-Looking Sonar operates in its near-field region and suggests certain solutions. The active sonar equation and its factors were explained and were evaluated for a realistic example of mine detection as well.

THIS PAGE INTENTIONALLY LEFT BLANK

TABLE OF CONTENTS

LIST OF FIGURES

LIST OF TABLES

ACKNOWLEDGMENTS

First and foremost, I must acknowledge the constant and unconditional support I received from my wife Athanasia Tasiopoulou during the whole two years of academic effort at the NPS. I would also like to express my gratitude to my advisor L. J. Ziomek for his guidance and explanations that led me to the completion of this Thesis. I also want to express my appreciation to my Co-advisor B. Denardo for his support and tolerance that helped me a lot to achieve my goals.

I also wish to dedicate this thesis to all the Greek, American and International colleagues that one way or another helped me during my stay in Monterey and honored me with their friendships.

THIS PAGE INTENTIONALLY LEFT BLANK

I. INTRODUCTION

A. SCOPE OF THE THESIS

This thesis concerns the analysis of Side-Looking Sonar (SLS) performance and its capabilities in various operational requirements. Side-Looking Sonar (also known as side-scan sonar) is well known for high quality, high resolution, ocean bottom imaging [1]. Hence it is used for bathymetric surveys, commonly called seafloor mapping, by almost all navies throughout the world and also for other naval operations. The correct usage of SLS for a specific application is dependent on the knowledge of the capabilities as well as the restrictions of SLS. In order to assist the average user of a SLS device, we shall attempt to establish a logical and systematic set of procedures that will help one design and analyze the performance of a SLS in order to satisfy different operational requirements.

In this thesis sufficient information on SLS parameters will be provided, to make it easy for the average naval officer to select the right design for the corresponding application. In our analysis we will focus mainly on military applications, but the same principles and formulas can definitely apply to any other non-military applications as well.

B. OPERATIONAL CAPABILITIES

There are various operational capabilities that a Side-Looking Sonar (SLS) can facilitate. Based on its high accuracy in ocean-bottom imaging, a SLS can rapidly survey large ocean areas for bottom and suspended sea mines or other kind of threats. It can also be used for search and rescue operations in deep or shallow waters. Side-Looking Sonar is currently used on Autonomous Underwater Vehicles (AUVs) in order to provide information about the seafloor (especially in shallow water) and help AUVs navigate underwater or locate mines and other objects of interest on the bottom of the sea. Generally speaking, SLS is considered to be a very useful device in littoral warfare operations [2].

1. Usage of Side-Looking Sonar in Littoral Warfare

In recent years, many small-size conflicts worldwide took place near shores [3]. As a consequence, the interests of almost all navies in the world shifted from the high

seas to the littoral regions and that fact motivated research in different fields concerning Littoral Warfare Operations. By definition, littoral regions incorporate shallow-water environments. Also, littoral operations incorporate various levels of landings and other kinds of operations that require the fleet to approach near to shore, therefore being exposed to the threat of minefields. Having said that, the necessity for accurate and fast survey of the ocean bottom prior to the implementation of almost any kind of littoral operation becomes obvious. Side-Looking Sonar can perform the above-mentioned task, and this is one reason for the importance of understanding the operation of a SLS system. In the years to come, it is likely that more littoral operations will take place and the usage of SLS will be even more highly valued.

2. Usage of Side-Looking Sonar in Mine Hunting

In late 1994, the Naval Undersea Warfare Center (Newport, Rhode Island) began a concept of configuring a commercial, off-the-shelf (COTS) side-scan sonar unit for use in a 21 inch diameter torpedo shell section [2]. In January of 1995, a number of side-scan sonar manufacturers were invited to demonstrate their respective systems [2]. Toward this end, a shallow-water mine field was deployed for system evaluation in Newport harbor. During the evaluation trials, SLS systems were operated under a wide variety of ranges, altitudes and tow speeds. Based on the results of the contest, there was the conclusion that there is such a sonar system, off-the shelf, that could detect all deployed targets with excellent fidelity and resolution. In the demonstration, the Klein sonar (manufactured by Klein Associates Inc.) proved capable of detecting even "stealth" mines such as the Italian manufactured Manta or the Swedish Rockan mines [2]. That contest demonstrated the capabilities of SLS in mine hunting and showed that in the future, Navies all over the world should consider SLS as their main tool against mine fields.

3. Usage of Side-Looking Sonar in Sea-Floor Mapping

Sea-floor mapping often comes to mind when dealing with geological research or seismological evaluations. However, sea-floor mapping can be very useful in military operations too. There are many cases where naval operations have to take place in littoral areas where either no sea-floor maps exist, or the ones that exist are not considered to be current, and therefore not accurate. In addition, since the sea floor is quite a dynamic

place, meaning that it changes all the time due to various reasons like earthquakes, undersea volcanoes, etc., there is a need for a naval task force to be able to perform bottom imaging in an accurate and fast manner. Side-Looking Sonar is a device that can facilitate that need during naval operations and provide data that can be evaluated and used by the appropriate staff in the decision making process. Nevertheless, the usage of SLS in non-military activities concerning sea-floor imaging is not to be underestimated since it includes searching for ship or plane wreckage that could prove quite useful for military aims, too.

4. Usage of Side-Looking Sonar on Autonomous Underwater Vehicles

Autonomous Underwater Vehicles (AUVs) have a variety of applications. Non-military ones are considered to be applications that concern oceanography, environmental monitoring and underwater resources studies [4]. The main military application is considered to be mine hunting. The fact is that since 1950, the US Navy has lost more ships to mines than to missiles, torpedoes or bombs [5]. Mines are cheap but can cause great damage and successfully deny fleet access. This motivates navies all over the world to enhance their mine countermeasures capabilities and create new and more efficient types of mines. It has been shown that AUVs equipped with SLS can detect almost all kinds of known mines, even in shallow waters [2]. For that reason, research is currently being performed in mine detection at many educational institutes (including NPS), companies and other private and public institutions. Side-Looking Sonars are considered the appropriate devices to equip AUVs and help them autonomously navigate using artificial intelligence processes and detect bottom mine-like objects in real time.

C. REMAINDER OF THE THESIS

The remainder of the Thesis is organized as follows.

Chapter II discusses the characteristic parameters of a SLS and presents brief explanations of their formulas based on the tutorial on SLS by Ziomek [6].

Chapter III presents graphs that illustrate the behavior of the parameters mentioned in Chapter II using values found in the literature. Furthermore, it analyzes the graphs and presents numerical examples that show how these graphs can be used from the point of view of a user or designer.

Chapter IV approaches the shallow water environment, giving a definition as to what is usually considered to be shallow water and the complications that could arise when a SLS operates in such an environment. Chapter IV presents a near-field beam pattern and discusses the various problems that usually arise when a SLS operates in its near-field region. It also presents two possible scenarios where a SLS that operates in shallow water can create a far-field beam pattern without doing beam steering and aperture focusing.

Chapter V describes the characteristic equation of the active sonar, since SLS is itself an active sonar, and discusses each element of it. Additionally, it presents a mine detection example using some characteristic values in an attempt to simulate a real case.

Chapter VI presents the conclusions of this thesis and also makes suggestions for further future research.

II. FUNDAMENTAL MODEL

In order to proceed with the analysis of a Side-Looking Sonar (SLS) design, we shall first clearly define the concepts and parameters with which we will deal later on in the analysis. This is an important issue because there are cases where the literature does not agree in various definitions, terms and/or symbols. The equations and definitions of terms used to describe a SLS in this thesis are based on the tutorial on SLS by Ziomek [6], which is based on the work by Bruce [7], Tomiyasu [8], and Ziomek [9].

In this thesis, a SLS will be modeled as a planar aperture lying in the *YZ* plane as shown in Fig. 1, where the *X* axis is cross-range, the *Y* axis is depth and the *Z* axis is down-range [6]. To be more specific, the SLS is modeled as a rectangular piston with sides of length L_y and L_z meters in the *Y* and *Z* directions, respectively, and is moving along the *Z* axis with constant speed *V* [6].

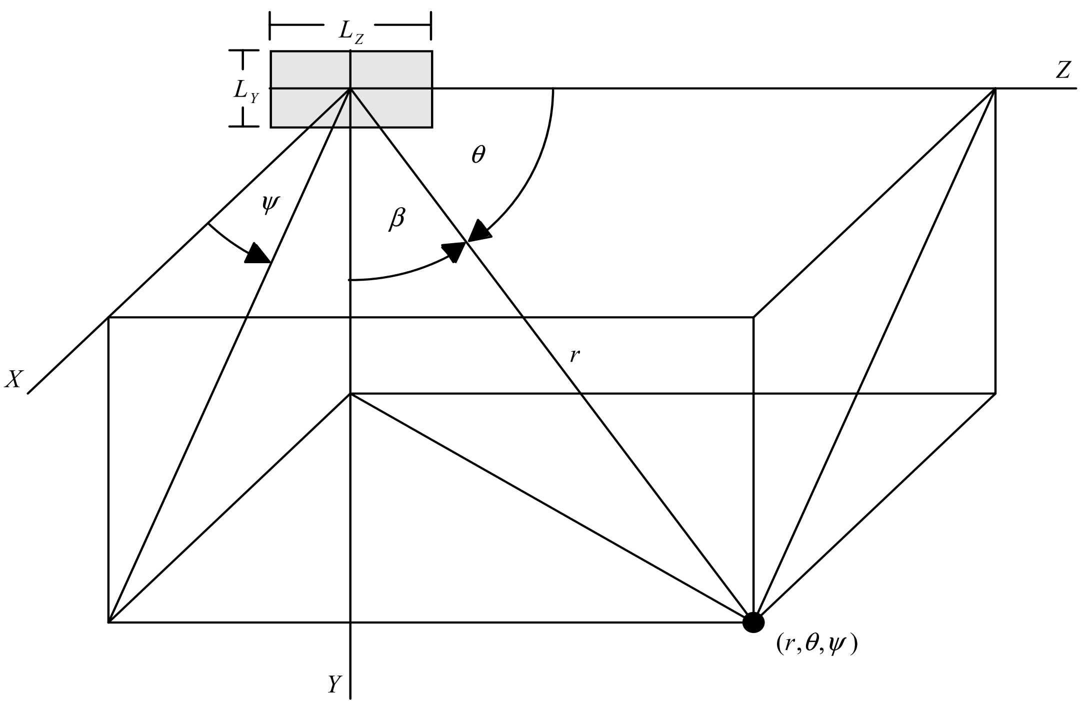

Figure 1. A SLS (planar aperture, rectangular in shape) lying in the YZ plane. Also shown is a field point in three-dimensional space with spherical coordinates (r,θ,ψ) as measured from the center of the aperture, and the angle β which is measured from the positive Y axis (After Ref. 6.)

A. SWATH WIDTH

Swath Width (*SW*) in meters, also referred to as the ground-plane swath width or the one-sided swath width, is a measure of the width of the area on the ocean bottom ensonified by the 3-dB beamwidth of the vertical, far-field beam pattern of a SLS , as shown in Figure 2 [6]. Concerning Figure 2, h is the height (altitude) of the center of the aperture above the ocean bottom in meters; ψ' (or β') is the beam-steer angle in degrees; $x_{\min}$ is the width of the blind zone in meters, also known as the width of the one-sided blind zone, or the cross-range coordinate of the beginning (near-edge) of the *SW*; $r_{\min}$ is the minimum slant-range in meters, corresponding to $x_{\min}$; $x_{\max}$ is the cross-range coordinate of the end (far-edge) of the *SW* in meters; and $r_{\max}$ is the maximum slant-range in meters corresponding to $x_{\max}$.

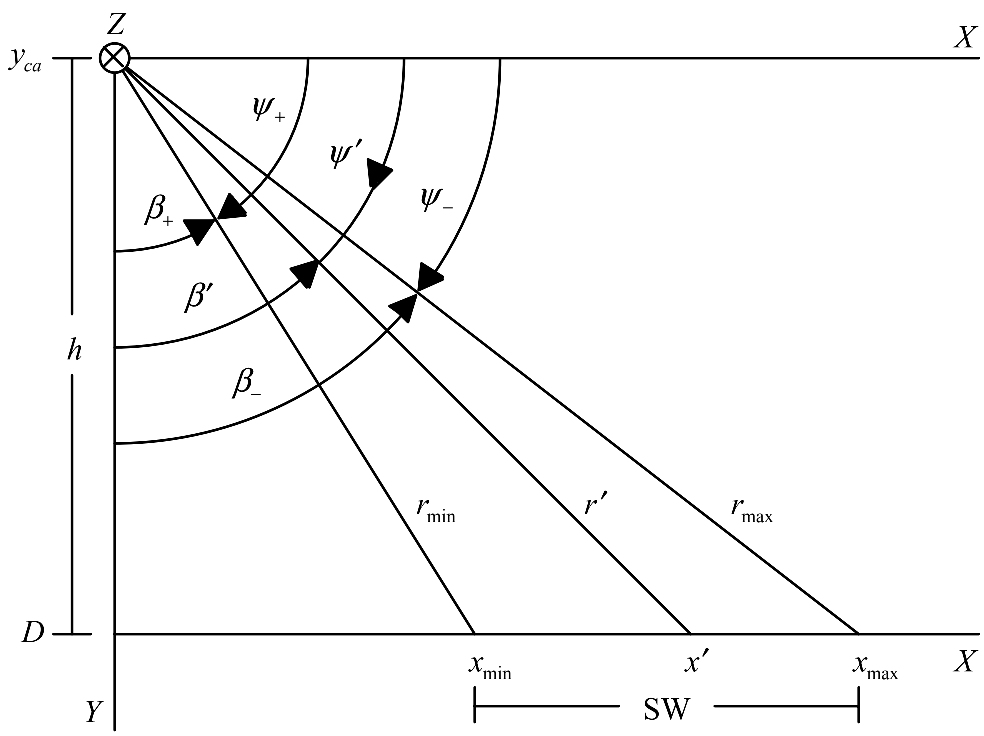

Figure 2. Angles involved in the derivation of the 3-dB beamwidth $\Delta\psi = \psi_+ - \psi_-$ (or $\Delta\beta = \beta_- - \beta_+$) of the vertical, far-field beam pattern in the XY plane. The parameters y_{ca} and D are the depths of the center of the aperture and the ocean, respectively. Also shown is the swath width $\text{SW} = x_{\max} - x_{\min}$ (After Ref. 6)

The equation used for *SW* in this thesis is from Ziomek [6] and is given by

$$SW = h\frac{\sin(\Delta\psi)}{\sin^2\psi' - \left(\frac{\Delta\nu}{2}\right)^2}, \quad 0° < \psi' < 90°, \quad \left|\sin\psi' \pm \frac{\Delta\nu}{2}\right| \le 1, \quad \sin\psi' > \frac{\Delta\nu}{2}, \tag{2.1}$$

where h is the height in meters of the center of the aperture above the ocean bottom, $\Delta\psi$ is the 3-dB beamwidth in degrees of the vertical, far-field beam pattern in the *XY* plane and is given by

$$\Delta\psi = \sin^{-1}(\sin\psi' + \frac{\Delta\nu}{2}) - \sin^{-1}(\sin\psi' - \frac{\Delta\nu}{2}), \qquad \left|\sin\psi' \pm \frac{\Delta\nu}{2}\right| \le 1, \tag{2.2}$$

ψ' is the beam-steer angle in degrees and $\Delta\nu$ is the dimensionless 3-dB beamwidth of the vertical, far-field beam pattern in direction-cosine space, which for the case of a rectangular piston is given by

$$\frac{\Delta\nu}{2} \approx 0.443\frac{\lambda}{L_y}. \tag{2.3}$$

In Chapter III of this thesis, we will present and discuss both tables and plots of $\frac{SW}{h}$ versus $\frac{x_{\min}}{h}$ for different values of the ratio $\frac{\lambda}{L_y}$. Toward that end, we need the following set of equations from Ziomek [6]:

$$\beta_+ = \tan^{-1}\left(\frac{x_{\min}}{h}\right), \tag{2.4}$$

$$\beta' = \cos^{-1}\left(\cos\beta_+ - \frac{\Delta\nu}{2}\right), \quad \left|\cos\beta_+ - \frac{\Delta\nu}{2}\right| \le 1, \tag{2.5}$$

and

$$\psi' = 90° - \beta'. \tag{2.6}$$

The ratio $\frac{x_{\min}}{h}$ affects the value of β_+ [see (2.4)] and the ratio $\frac{\lambda}{L_y}$ affects the value of $\frac{\Delta\nu}{2}$ [see (2.3)]. Both β_+ and $\frac{\Delta\nu}{2}$ affect the value of β' [see (2.5)], which affects the values of ψ' [see (2.6)], then $\Delta\psi$ [see (2.2)], and finally $\frac{SW}{h}$ [see (2.1)].

B. ALONG-TRACK (AZIMUTHAL) RESOLUTION

Sample Along-Track resolution Δz in meters is a measure of the width of the area on the ocean bottom at slant-range r and cross-range x ensonified by the 3-dB beamwidth of the horizontal, far-field beam pattern of a SLS in the *XZ* plane (see Figure 3) [6]. The along-track (azimuthal) resolutions at cross-ranges $x_{\min}$ (the beginning or near-edge of the SW) and $x_{\max}$ (the end or far-edge of the SW) are given by Figures 3 and 4 [6],

$$\Delta z_{\min} = 2x_{\min} \tan\left(\frac{\Delta\theta}{2}\right) \tag{2.7}$$

and

$$\Delta z_{\max} = 2x_{\max} \tan\left(\frac{\Delta\theta}{2}\right), \tag{2.8}$$

respectively, where $x_{\min}$ and $x_{\max}$ are given by

$$x_{\min} = h\cot\psi_+ = h\tan\beta_+ \tag{2.9}$$

and

$$x_{\max} = h\cot\psi_- = h\tan\beta_- , \tag{2.10}$$

respectively. The parameter $\Delta\theta$ is the 3-dB beamwidth in degrees of the horizontal, far-field beam pattern in the *XZ* plane given by Figure 5 [6]

$$\Delta\theta = 2\sin^{-1}\left(\frac{\Delta w}{2}\right), \qquad \frac{\Delta w}{2} \le 1, \tag{2.11}$$

where *Δw* is the dimensionless 3-dB beamwidth of the horizontal, far-field beam pattern in direction-cosine space, which for the case of a rectangular piston is given by

$$\frac{\Delta w}{2} \approx 0.443\frac{\lambda}{L_Z}. \tag{2.12}$$

In Chapter III of this thesis, we will also present and discuss both tables and plots of $\Delta\theta$ versus $\frac{\Delta z_{\min}}{x_{\min}}$. Toward that end, solving for $\Delta\theta$ using (2.7) yields

$$\Delta\theta = 2\tan^{-1}\left(\frac{\Delta z_{\min}}{2x_{\min}}\right). \tag{2.13}$$

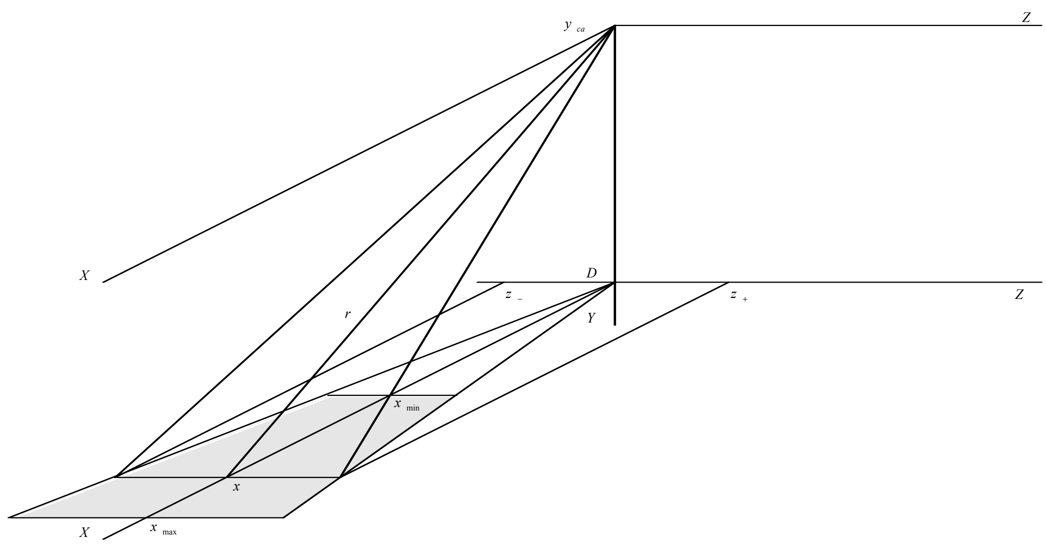

Figure 3. Along-track (azimuthal) resolution $\Delta z = z_+ - z_-$ at slant-range r and cross-range x. The shaded area represents the area on the ocean bottom within the swath width $\mathrm{SW} = x_{\max} - x_{\min}$ ensonified by the 3-dB beamwidth of the horizontal, far-field beam pattern in the XZ plane (After Ref. 6).

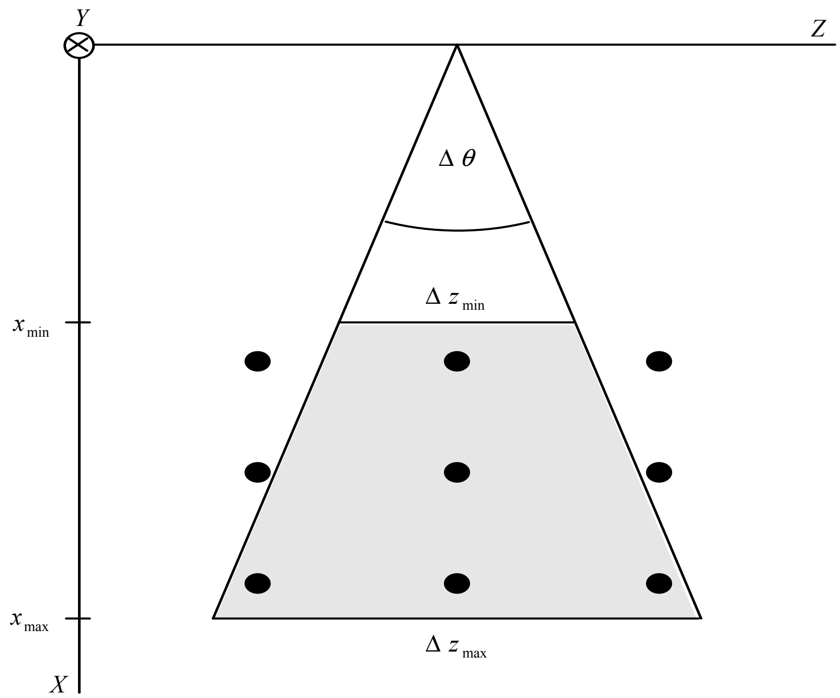

Figure 4. For a given value of horizontal, 3-dB beamwidth $\Delta\theta$, the ability of a SLS to resolve closely-spaced points on the ocean bottom decreases as the cross-range increases (After Ref. 6).

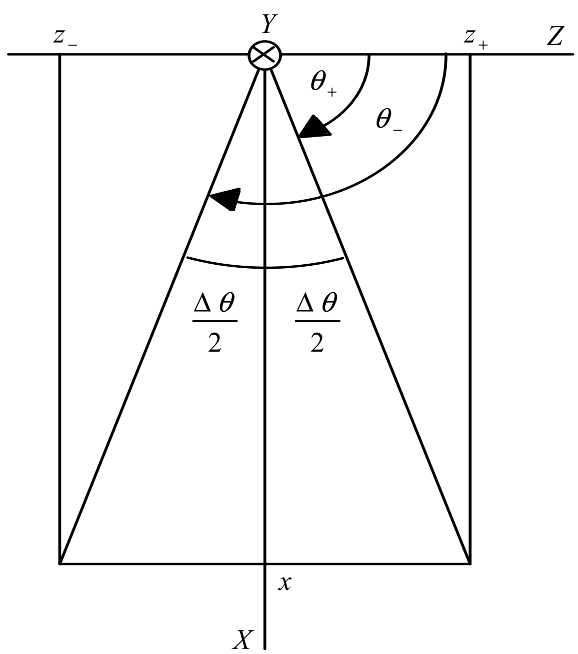

Figure 5. Angles involved in the derivation of the 3-dB beamwidth $\Delta\theta$ of the horizontal, far-field beam pattern in the XZ plane (After Ref. 6).

C. FAR-FIELD (FRAUNHOFER) REGION REQUIREMENTS

All the above mentioned formulas/equations are based on operating a SLS in the far-field. In order to be guaranteed that the far-field beam pattern of a SLS will ensonify a point on the ocean bottom at the minimum slant range $r_{\min}$, $r_{\min}$ must satisfy the following inequality [6]:

$$r_{\min} > \pi \frac{L_y^2 + L_z^2}{4\lambda} > 0.678\sqrt{L_y^2 + L_y^2} \ . \tag{2.14}$$

From Figure 2 it can be seen that the minimum slant-range $r_{\min}$ corresponds to the beginning of the SW at $x_{\min}$. Also, from the geometry of Figure 2 and using the Pythagorean theorem, the altitude h is given by

$$h = \sqrt{r_{\min}^2 - x_{\min}^2} \ . \tag{2.15}$$

Therefore, another requirement for the minimum slant-range $r_{\min}$ is

$$r_{\min} > x_{\min} \tag{2.16}$$

so that h is a real number.

It is possible that if a SLS is required to operate in shallow water environments the above mentioned criteria for the far-field region will not be satisfied. In Chapter IV we will discuss such cases in more detail. For now, we will model the operation of a SLS in the far-field region using the above mentioned design equations.

For a shallow water design, valid in the far-field region of a SLS, we need the following additional equations [6]:

$$L_z \approx \frac{1}{f}\frac{0.443c}{\sin\left(\Delta\theta/2\right)}. \tag{2.17}$$

where f is the operating frequency of the SLS in Hertz, c is the speed of sound in seawater in m/sec, and $\Delta\theta$ is given by (2.13), and from (2.14), we can also derive the following useful design equation

$$L_y < \sqrt{\frac{4c}{\pi f}r_{\min} - L_z^2} \ . \tag{2.18}$$

D. CHAPTER SUMMARY

In this chapter we presented the characteristic parameters of a SLS and the equations that rule their operation. Furthermore, we stated the requirements needed for these equations to be valid. Next, in Chapter III, we evaluate these equations using Matlab software and examine the capabilities and limitations of a SLS based on the produced plots and tables. Additionally, we will determine the values of characteristic parameters of a SLS for various scenarios.

III. PERFORMANCE ANALYSIS OF A SLS

This Chapter presents a performance analysis of a SLS in different operational conditions and also present numerical examples based on the produced plots and tables.

A. RATIO OF SWATH WIDTH OVER HEIGHT

In an effort to analyze the performance of a SLS, it was decided to begin by evaluating the ratio of swath width to height, $\frac{SW}{h}$, versus the ratio of the width of the one-sided blind zone to the height, $\frac{x_{\min}}{h}$, for different fixed values of the ratio of the wavelength to the aperture length in the Y direction, $\frac{\lambda}{L_y}$. The usage of these ratios helps to demonstrate the trade offs between the ocean-bottom area that is necessary to be surveyed versus the value of the one sided-blind zone that we should expect at a specific height (altitude) in conjunction with the frequency that should be used by a SLS of a specific length in the Y direction. In the case where there is not an already manufactured SLS, then the ratio $\frac{SW}{h}$ can be used for designing purposes.

The ratio $\frac{SW}{h}$ is given by (2.1) through (2.6). Figures 6, 7, 9 and 10 are plots of $\frac{SW}{h}$ versus $\frac{x_{\min}}{h}$ for $\frac{\lambda}{L_y}$ equal to 0.25, 0.5, 0.75 and 1, respectively. The range of values used for the ratio $\frac{x_{\min}}{h}$ is between 0 and 2, which are considered to be typical values found in the literature ([7], [10]), with a step-size of 0.01 (1%). The data used in the figures are in Tables 1 through 4, respectively, in the Appendix.

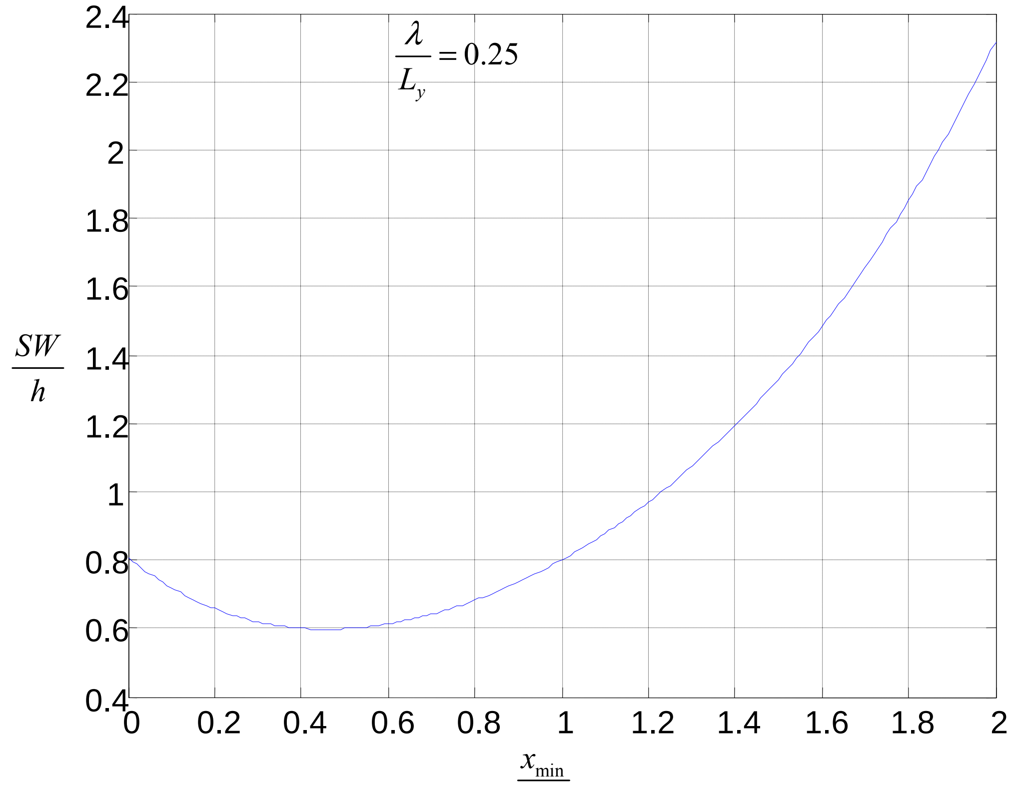

Figure 6. Ratio SW/h versus $x_{\min}/h$ for $\lambda/L_y = 0.25$. The actual values can be found in the Appendix in Table 1.

It is important to note that in Figure 6 we observe that for $\frac{x_{\min}}{h}$ between **0** and **0.46,** the ratio $\frac{SW}{h}$ decreases, and after the value **0.47** for the ratio $\frac{x_{\min}}{h}$, the values of the ratio $\frac{SW}{h}$ increase. The behavior of the ratio $\frac{SW}{h}$ in Figure 6 can cause a certain amount of confusion since it is unique among our plots and should be taken under consideration when a SLS with a value of 0.25 for the ratio $\frac{\lambda}{L_y}$ is desired to be designed.

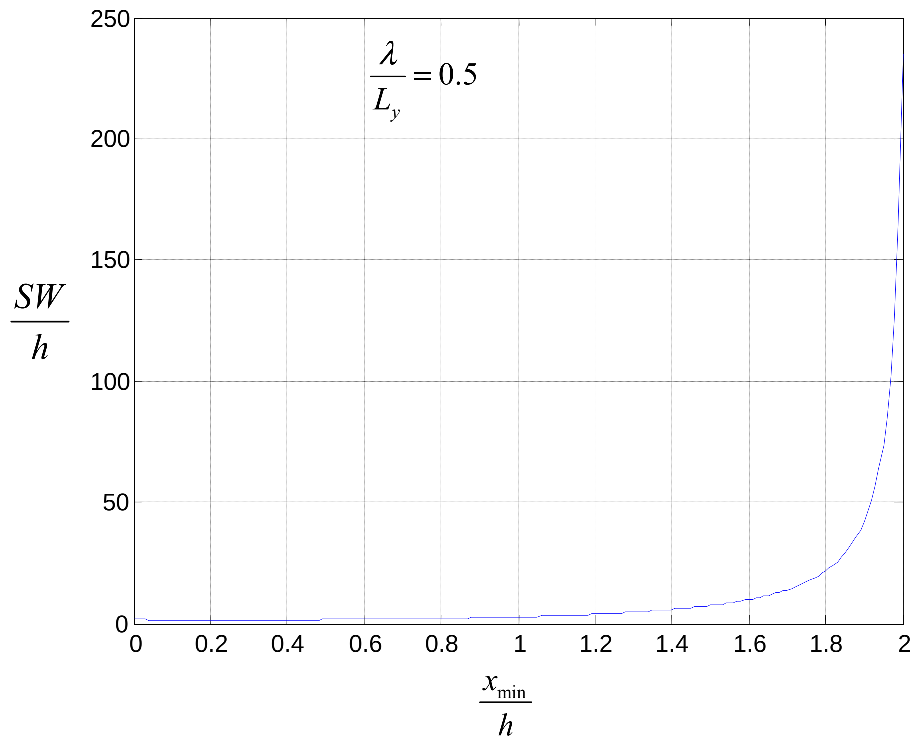

Figure 7. Ratio SW/h versus $x_{\min}/h$ for $\lambda/L_y = 0.5$. The actual values can be found in the Appendix in Table 2.

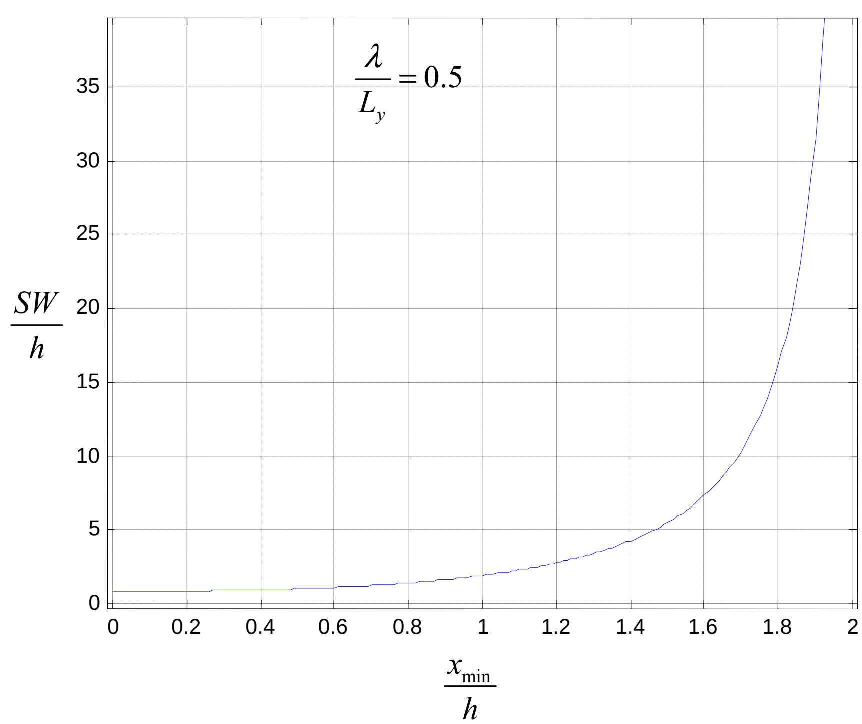

Figure 8. Magnification of the Y axis in Figure 7 in order to better display the range of values produced for SW/h when $x_{\min}/h$ has values between 0 and 1.8.

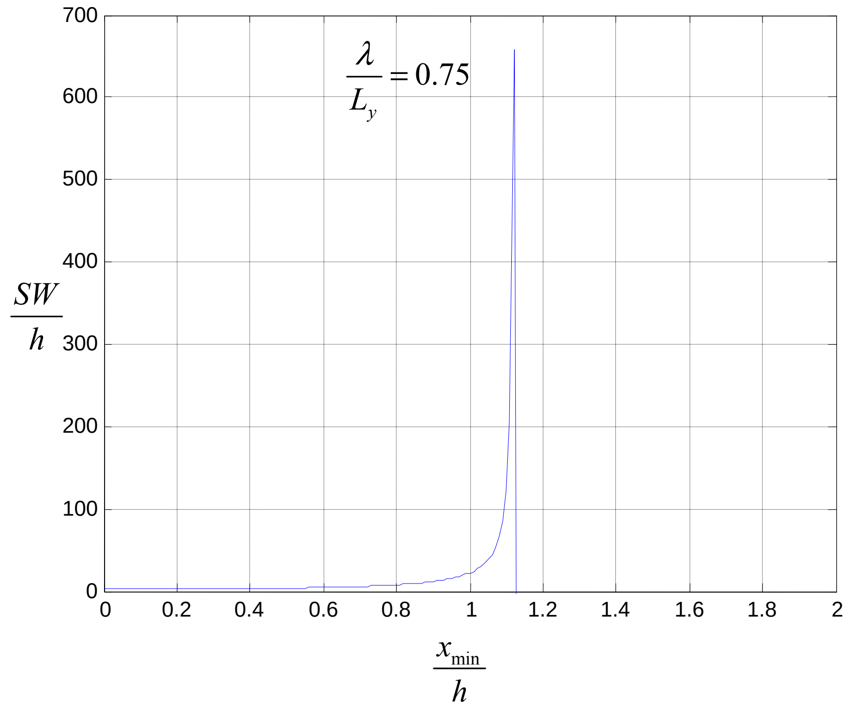

Figure 9. Ratio SW/h versus $x_{\min}/h$ for $\lambda/L_y = 0.75$. The actual values can be found in the Appendix in Table 3.

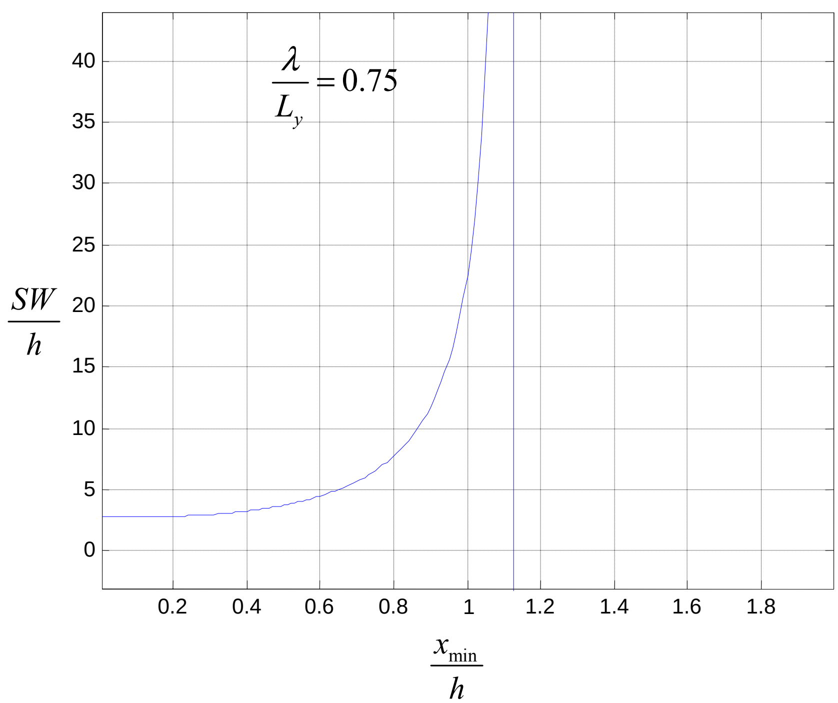

Figure 10. Magnification of the Y axis in Figure 9 in order to better display the range of values produced for SW/h when $x_{\min}/h$ has values between 0 and 1.

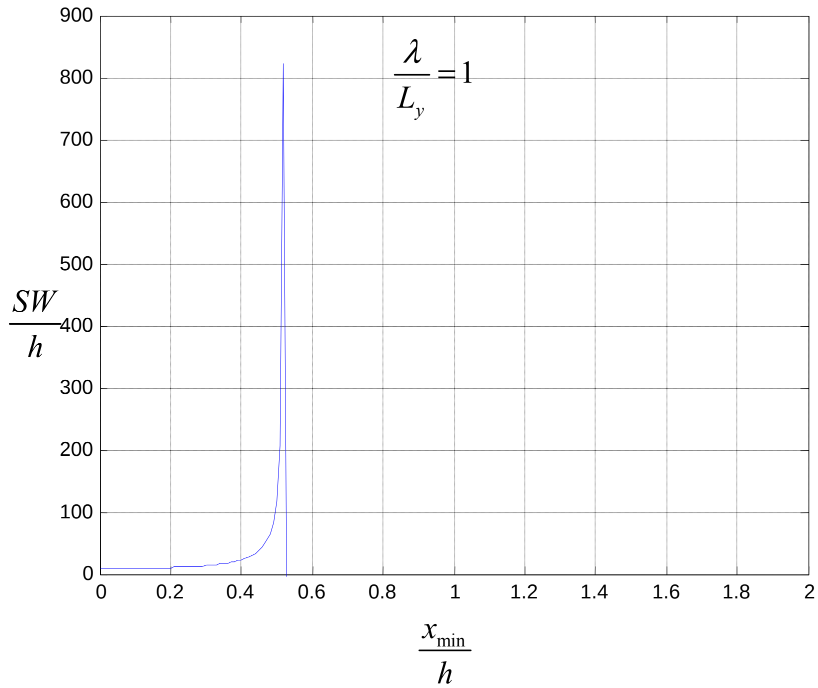

Figure 11. Ratio SW/h versus $x_{\min}/h$ for $\lambda/L_y = 1$. The actual values can be found in the Appendix in Table 4.

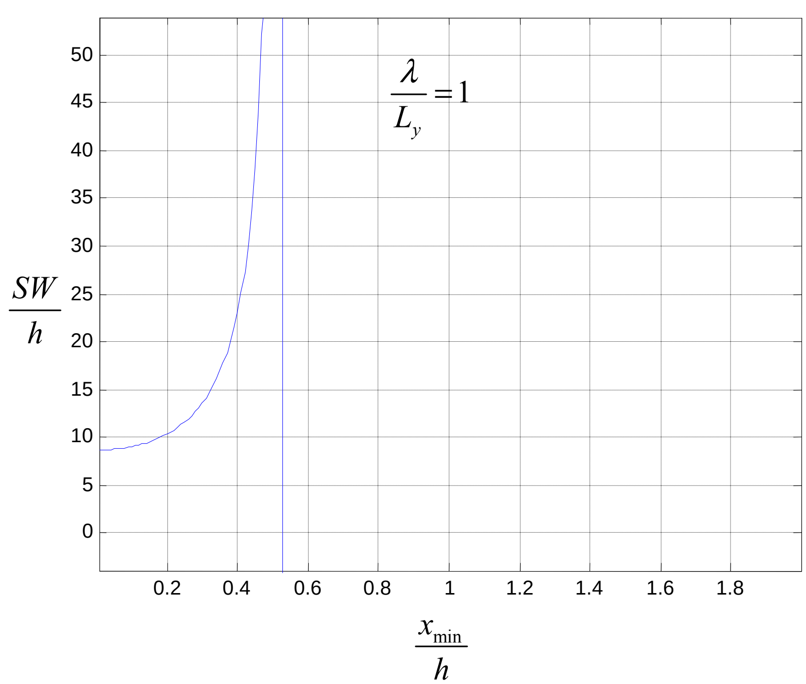

Figure 12. Magnification of the Y axis in Figure 11 in order to better display the range of values produced for SW/h when $x_{\min}/h$ has values between 0 and 0.4.

Before we discuss Figures 6 through 12 in detail, let us define the Area Coverage Rate (*ACR*), since it will be used for the analysis of the figures.

1. Area Coverage Rate

Area coverage rate (*ACR*), also referred to as survey coverage rate, is the amount of area surveyed by a SLS per unit of time. The formula for *ACR* in m^2/sec, is given by (see Figure 2)

$$ACR = SW \times V \tag{3.1}$$

where V is the constant speed of the platform in m/sec and *SW* is the swath width in meters. In many cases it is desired to increase the *ACR* in order to survey bigger areas in less time. Such a result can be achieved by increasing the platform's speed, increasing the *SW,* or both [6].

B. ANALYSIS

By observing Figures 6 through 12, the following two comments can be made:

First, as the ratio $\frac{\lambda}{L_y}$ increases (from 0.25 to 1), the ratio $\frac{SW}{h}$ increases for a given value of $\frac{x_{\min}}{h}$. For example, from Figure 6 (and Table 1), when $\frac{x_{\min}}{h}$ equals **0.2** the ratio $\frac{SW}{h}$ is approximately **0.65**. However, from Figure 8 (and Table 2), when $\frac{x_{\min}}{h} = 0.2$, then $\frac{SW}{h} \approx 1.3$. Furthermore, from Figure 10 (and Table 3) when $\frac{x_{\min}}{h} = 0.2$ then $\frac{SW}{h} \approx 2.8$ and finally, from Figure 12 (and Table 4), when $\frac{x_{\min}}{h} = 0.2$ then $\frac{SW}{h} \approx 10$. This result is quite desirable (and not surprising) since it implies large values for the *SW*, and consequently, large values for the *ACR.* As was mentioned, this result is actually not surprising since as the ratio $\frac{\lambda}{L_y}$ increases (from 0.25 to 1) the 3-dB beamwidth $\Delta\psi$ of the vertical beam pattern increases so it is capable of surveying bigger areas on the ocean bottom. This is indicated by the fact that the ratio $\frac{SW}{h}$ increases. Plots

of the 3-dB beamwidth of the vertical beam pattern versus $\frac{x_{\min}}{h}$ for different values of $\frac{\lambda}{L_y}$ will be presented later. Furthermore, we would expect that the beam-steer angle ψ' should decrease in value as the vertical beamwidth increases. This result will be shown when we present beam-steer angle plots versus $\frac{x_{\min}}{h}$ for different values of $\frac{\lambda}{L_y}$.

Second, in Figures 11 and 12, the ratio $\frac{SW}{h}$ abruptly drops to zero when $\frac{x_{\min}}{h} \geq 1.13$ in Figure 11 and when $\frac{x_{\min}}{h} \geq 0.53$ in Figure 12. This occurs when the ratio $\frac{SW}{h}$ becomes negative and therefore has no physical meaning. From (2.1) it can be seen that $\frac{SW}{h}$ becomes negative when $\sin\psi' < \frac{\Delta\nu}{2}$. We can observe from Figures 6 through 12 that this limitation becomes greater as we increase the ratio $\frac{\lambda}{L_y}$. This phenomenon poses a limit on our ability to use arbitrary ratios of wavelength over aperture length in the *Y* direction. Indeed for $\frac{\lambda}{L_y} > 1.128$, the ratio $\frac{SW}{h}$ is negative for any value of the ratio $\frac{x_{\min}}{h}$ between 0 and 2.

C. NUMERICAL APPLICATION

Using Figures 6 through 12 and their corresponding tables, some of the parameters of a SLS can be determined. For example, if we have an already manufactured SLS with known length in the *Y* direction L_y, and operating frequency *f*, we can estimate what the *SW* will be for a given height (altitude) *h*, and for a desired width of the one-sided blind zone $x_{\min}$. A numerical application of such a scenario would be a SLS with $L_y = 0.1\,\text{m}$ and $\lambda = 0.05\,\text{m}$ (corresponding to an operational frequency $f = 30$ kHz), so that $\frac{\lambda}{L_y} = 0.5$. If it is desired to operate at an altitude $h = 50$

m with width of the one-sided blind zone $x_{\min} = 10$ m, then $\frac{x_{\min}}{h} = 0.2$. Using Figure 7 ($\frac{\lambda}{L_y}$ = 0.5) and the corresponding Table 2, we find $\frac{SW}{h}$ = 1.3685, so *SW* = 68.425 m. If the estimated *SW* is considered to be too small and the user is not allowed to change the ratio $\frac{x_{\min}}{h}$, then a solution would be to increase the ratio $\frac{\lambda}{L_y}$ by decreasing the operational frequency. For operational frequency $f = 15$ kHz, we have $\lambda = 0.1$ m and $\frac{\lambda}{L_y} = 1$, so Figure 12 and its corresponding Table 4 can be used, where for $\frac{x_{\min}}{h} = 0.2$, $\frac{SW}{h} = 10.3256$, and as result, for $h = 50$ m, the *SW* is estimated to be 516.28 m. It can be seen that with $\frac{\lambda}{L_y} = 1$, the *SW* is approximately 654% larger than in the previous scenario ($\frac{\lambda}{L_y} = 0.5$) and the only parameter that was actually changed was the operational frequency. However, if the user wanted to keep the initial ratio $\frac{\lambda}{L_y} = 0.5$ fixed and still wanted to increase the *SW*, then a solution would be to increase the ratio $\frac{x_{\min}}{h}$. For example, for $x_{\min} = 20$ m and all other parameters unchanged, then $\frac{x_{\min}}{h} = 0.4$ and from Table 2 we can observe that $\frac{SW}{h} = 1.4008$; consequently, the $SW = 70.04$ m, which is a slight increase (approximately 2%) compared to the initial value of 68.425 m.

D. BEAMWIDTH $\Delta\psi$ VERSUS $\frac{x_{\min}}{h}$

The next step in the performance analysis of a SLS will be the presentation of plots of the 3-dB beamwidth of the vertical beam pattern $\Delta\psi$, versus the ratio of the width of the one-sided blind zone over the height $\frac{x_{\min}}{h}$, for different fixed values of the

ratio of the wavelength over the aperture length in the Y direction, $\frac{\lambda}{L_y}$. The 3-dB beamwidth of the vertical beam pattern $\Delta\psi$, is given in degrees by (2.2) through (2.6). Figures 13 through 16 are plots of $\Delta\psi$ versus $\frac{x_{\min}}{h}$ for $\frac{\lambda}{L_y}$ equal to 0.25, 0.5, 0.75 and 1, respectively. The range of values used for the ratio $\frac{x_{\min}}{h}$ is again between 0 and 2 which are considered to be typical values found in the literature ([7], [10]), with a step-size of 0.01 (1%). The data used in the figures are in Tables 5 through 8, respectively, in the Appendix.

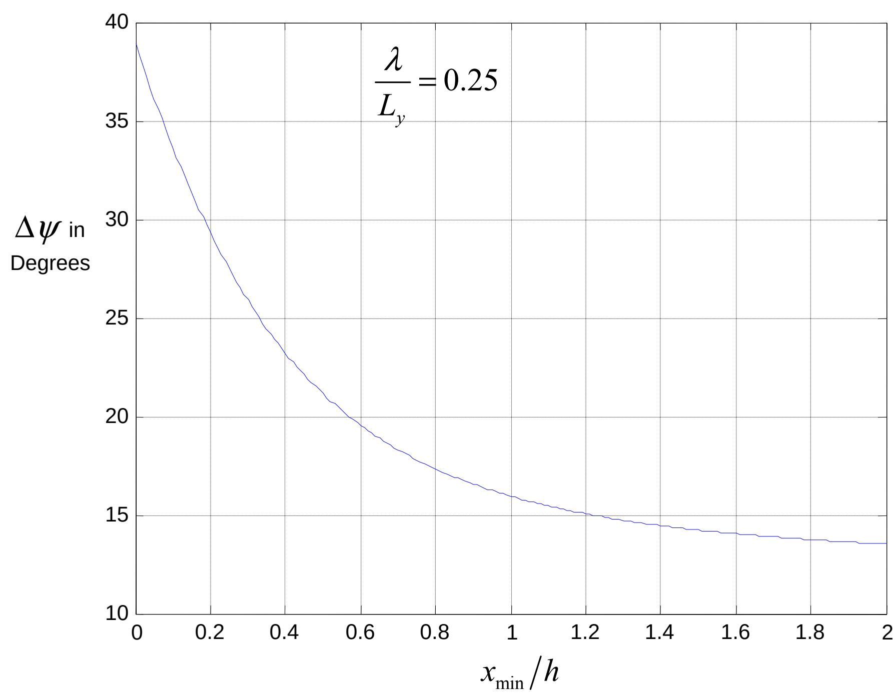

Figure 13. Three-dB beamwidth of the vertical, far-field beam pattern versus $x_{\min}/h$ for λ/L_y = 0.25. The actual values can be found in the Appendix in Table 5.

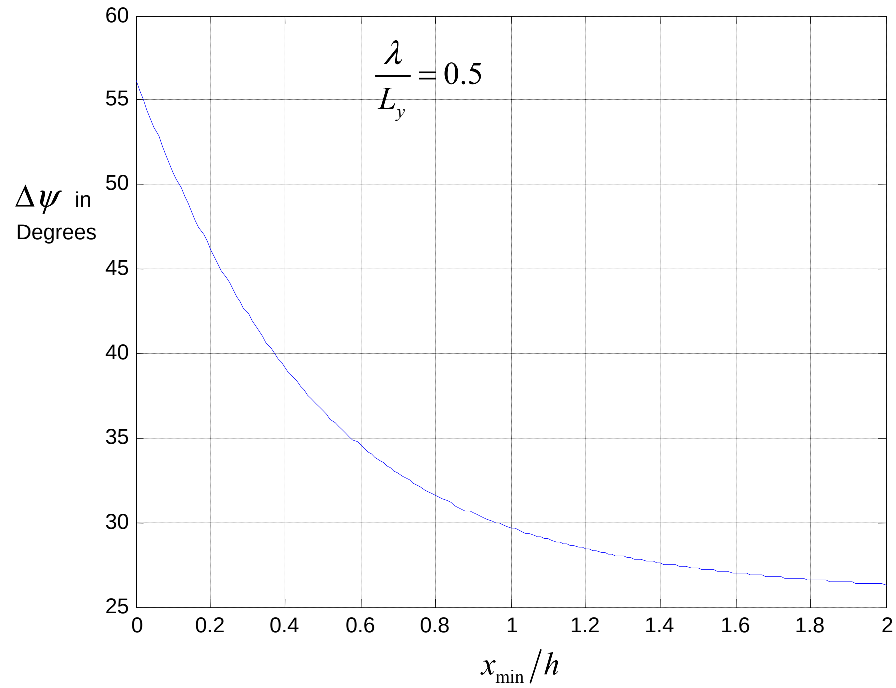

Figure 14. Three-dB beamwidth of the vertical, far-field beam pattern versus $x_{\min}/h$ for $\lambda/L_y = 0.5$. The actual values can be found in the Appendix in Table 6.

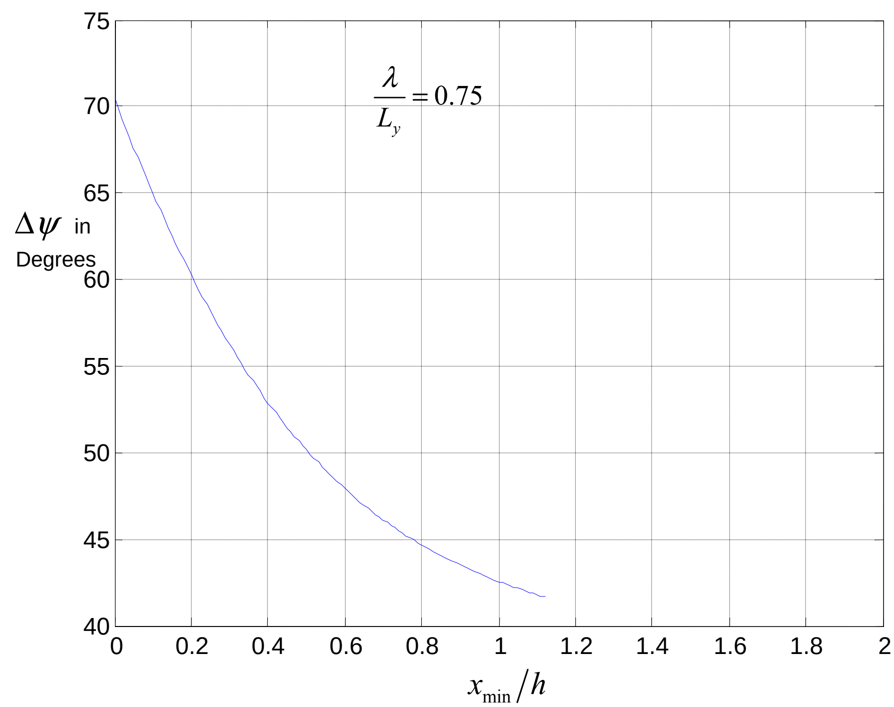

Figure 15. Three-dB beamwidth of the vertical, far-field beam pattern versus $x_{\min}/h$ for $\lambda/L_y = 0.75$. The actual values can be found in the Appendix in Table 7.

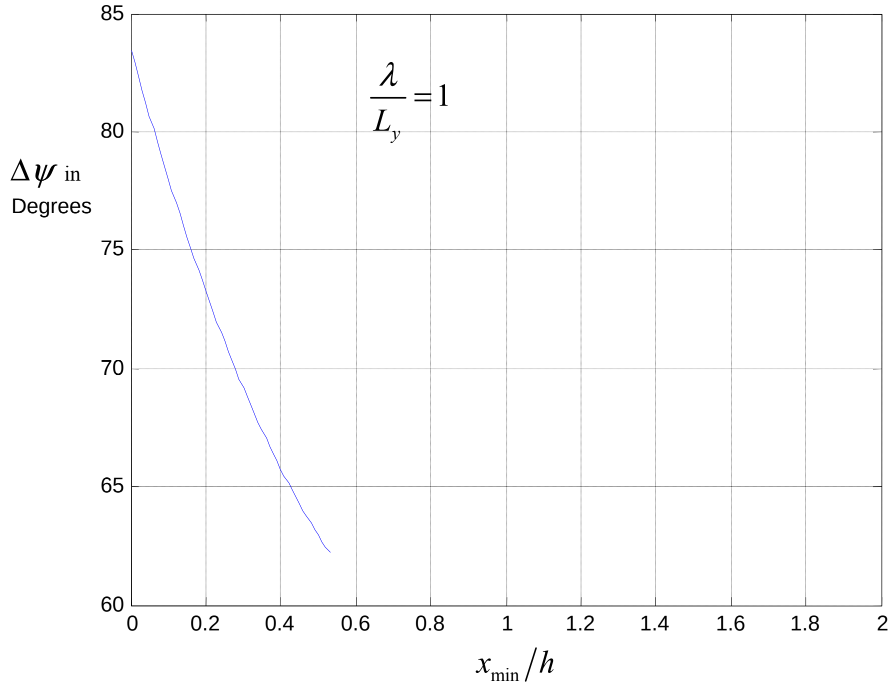

Figure 16. Three-dB beamwidth of the vertical, far-field beam pattern versus $x_{\min}/h$ for λ/L_y = 1. The actual values can be found in the Appendix in Table 8.

E. ANALYSIS

By observing Figures 13 through 16 the following two comments can be made:

First, as the ratio $\dfrac{\lambda}{L_y}$ increases (from 0.25 to 1), the 3-dB beamwidth $\Delta\psi$ of the vertical, far-field beam pattern increases, as well, for any given value of $\dfrac{x_{\min}}{h}$. For example, from Figure 13 (and Table 5), when $\dfrac{x_{\min}}{h}$ equals **0.2,** $\Delta\psi$ is approximately **29.3°**. However, from Figure 14 (and Table 6), when $\dfrac{x_{\min}}{h} = 0.2$, then $\Delta\psi \approx 46.1°$. Furthermore, from Figure 15 (and Table 7), when $\dfrac{x_{\min}}{h} = 0.2$, then $\Delta\psi \approx 60.2°$ and finally, from Figure 16 (and Table 8), when $\dfrac{x_{\min}}{h} = 0.2$, then $\Delta\psi \approx 73.2°$. The fact that

the 3-dB beamwidth $\Delta\psi$ of the vertical, far-field beam pattern increases as the ratio $\frac{\lambda}{L_y}$ increases implies that a SLS would be more efficient in surveying large ocean-bottom areas at bigger ratios of $\frac{\lambda}{L_y}$, rather than smaller. That conclusion was also derived by the $\frac{SW}{h}$ (see Figures 6 through 12). Furthermore, it would be expected that as the 3-dB beamwidth $\Delta\psi$ increases, smaller values of beam-steer angle ψ'**,** would be required for a SLS to survey a fixed ocean-bottom area. This result will be shown later in the beam-steer angle plots versus $\frac{x_{\min}}{h}$ for different values of $\frac{\lambda}{L_y}$.

Second, in Figures 15 and 16, the 3-dB vertical beamwidth plots are being terminated at the same values of $\frac{x_{\min}}{h}$ as the plots of $\frac{SW}{h}$ (see Figures 10 and 12). This is required to be done although (2.2) seems unaffected by the inequalities of (2.1). However, when the inequalities of (2.1) violated, the produced result in any parameter of a SLS would have no physical meaning whatsoever. For that reason the plots terminated when $\frac{x_{\min}}{h} \geq 1.13$ in Figure 15, and $\frac{x_{\min}}{h} \geq 0.53$ in Figure 16.

F. BEAM-STEER ANGLE ψ' VERSUS $\frac{x_{\min}}{h}$

Another useful set of plots that will be presented at this point is the beam-steer angle ψ' versus the ratio of the width of the one-sided blind zone over the height $\frac{x_{\min}}{h}$, for different fixed values of the ratio of the wavelength over the aperture length in the *Y* direction, $\frac{\lambda}{L_y}$. The beam-steer angle ψ' is given in degrees by (2.3) through (2.6). Figures 17 through 20 are plots of ψ' versus $\frac{x_{\min}}{h}$ for $\frac{\lambda}{L_y}$ equal to 0.25, 0.5, 0.75 and 1, respectively. The range of values used for the ratio $\frac{x_{\min}}{h}$ is again between 0 and 2, which

are considered to be typical values found in the literature ([7], [10]), with a step-size of 0.01 (1%). The data used in the figures are in Tables 9 through 12, respectively, in the Appendix.

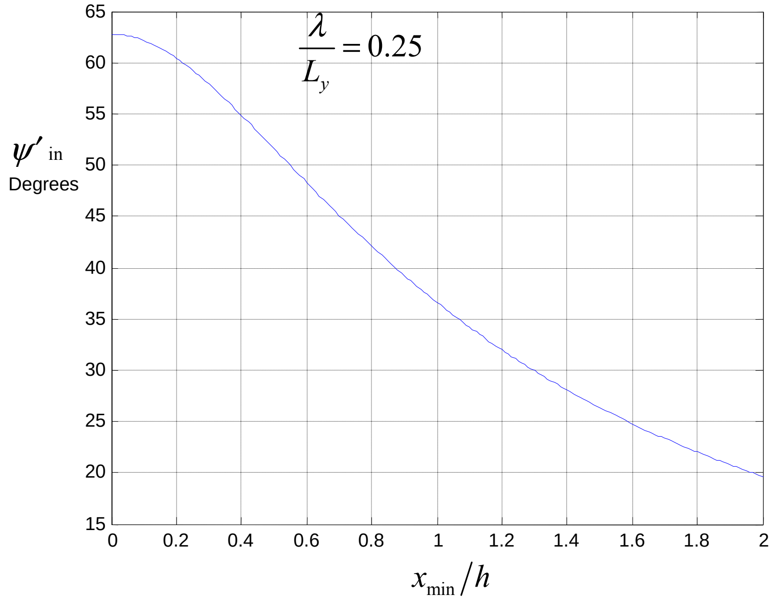

Figure 17. Beam-steer angle ψ' in degrees, versus $x_{\min}/h$ for λ/L_y = 0.25. The actual values can be found in the Appendix in Table 9.

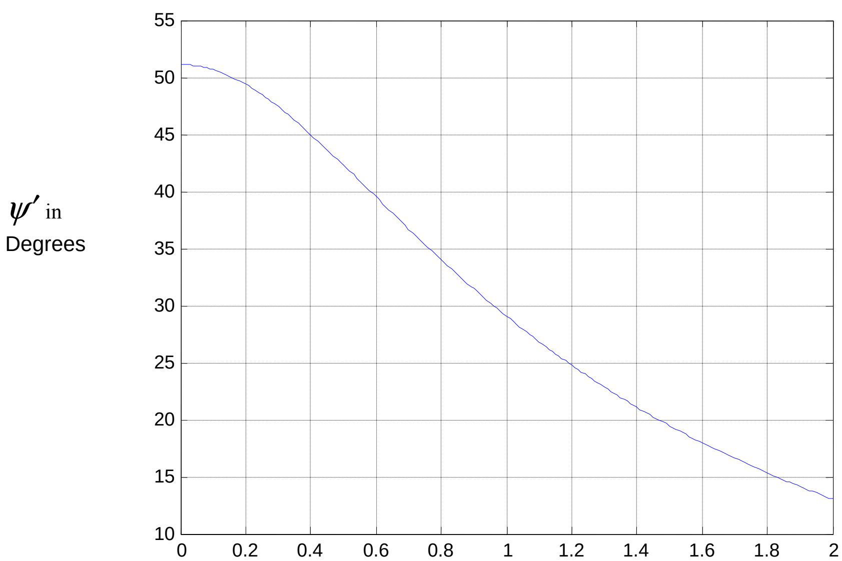

Figure 18. Beam-steer angle ψ' in degrees, versus $x_{\min}/h$ for λ/L_y = 0.5. The actual values can be found in the Appendix in Table 10.

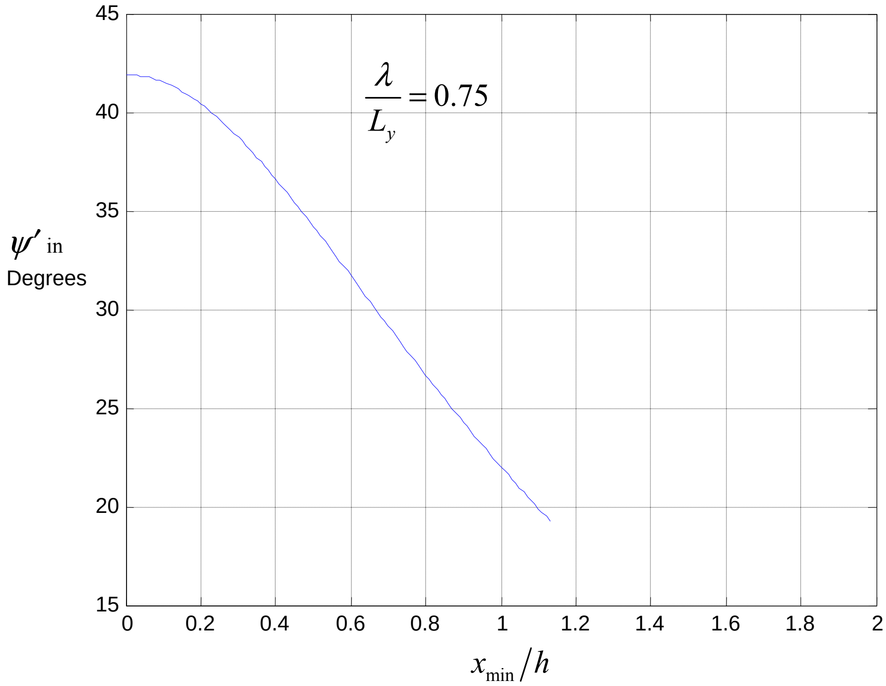

Figure 19. Beam-steer angle ψ' in degrees, versus $x_{\min}/h$ for $\lambda/L_y = 0.75$. The actual values can be found in the Appendix in Table 11.

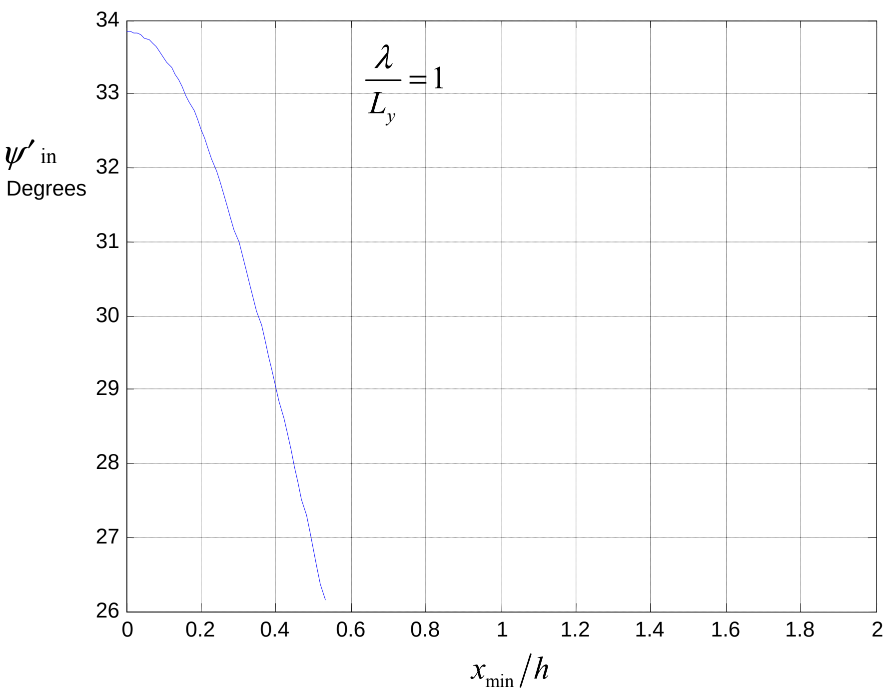

Figure 20. Beam-steer angle ψ' in degrees, versus $x_{\min}/h$ for $\lambda/L_y = 1$. The actual values can be found in the Appendix in Table 12.

G. ANALYSIS

By observing Figures 17 through 20 the following two comments can be made:

First, as the ratio $\frac{\lambda}{L_y}$ increases (from 0.25 to 1), the beam-steer angle ψ' decreases for any given value of $\frac{x_{\min}}{h}$. For example, from Figure 17 (and Table 9), when $\frac{x_{\min}}{h}$ equals **0.2,** ψ' is approximately **60.4°**. However, from Figure 18 (and Table 10), when $\frac{x_{\min}}{h} = 0.2$, then $\psi' \approx 49.3°$. Furthermore, from Figure 19 (and Table 11), when $\frac{x_{\min}}{h} = 0.2$, then $\psi' \approx 40.4°$ and finally, from Figure 20 (and Table 12), when $\frac{x_{\min}}{h} = 0.2$, then $\psi' \approx 32.5°$. The decrease of the beam-steer angle is in agreement with our results from the $\frac{SW}{h}$ plots and the 3-dB beamwidth of the vertical, far-field beam pattern, $\Delta\psi$, plots versus $\frac{x_{\min}}{h}$ for different values of $\frac{\lambda}{L_y}$. Indeed a SLS will require a smaller beam-steer angle in order to survey a given amount of ocean bottom area if its vertical beamwidth is increased. It has been shown that as the SLS's 3-dB beamwidth of the vertical, far-field beam pattern increases, the *SW* will increase too. That fact will make a SLS capable of surveying bigger areas of the ocean bottom in less time.

Second, in Figures 19 and 20, the beam-steer angle plots are terminated at the same values of $\frac{x_{\min}}{h}$ as the plots of $\frac{SW}{h}$ (see Figures 10 and 12), as is the 3-dB beamwidth of the vertical, far-field beam pattern $\Delta\psi$, versus $\frac{x_{\min}}{h}$ plots (see Figures 17 and 18). This is required to be done, although (2.6) seems unaffected by the inequalities of (2.1), because when the inequalities of (2.1) are violated, the produced result in any parameter of a SLS would have no physical meaning. For that reason the plots are terminated when $\frac{x_{\min}}{h} \geq 1.13$ in Figure 19, and $\frac{x_{\min}}{h} \geq 0.53$ in Figure 20.

H. NUMERICAL EXAMPLES

Having presented many of the basic parameters and their corresponding plots (see Figures 6 through 20) of a SLS's operation in the far-field region, numerical examples can now be given, that will show how these plots can be used on behalf of a user or a designer. Suppose that a user has an already manufactured SLS which has a fixed size in the *Y* direction L_y, equal to 0.2 m, and wants to operate it at height *h*, of 100 m. Furthermore, the user wants to achieve a *SW* approximately equal to 150 m and also wants the width of the one-sided blind zone $x_{\min}$, to be equal to 55 m. Using these numbers, the user creates the following ratios of $\frac{SW}{h} \approx 1.5$ and $\frac{x_{\min}}{h} = 0.55$. By looking in Tables 1 through 4, the user finds that only with a ratio $\frac{\lambda}{L_y} = 0.5$ can such a performance be achieved. Since the user knows the length in the *Y* direction, the wavelength and hence the frequency can also be determined, which comes out to be 15 kHz. Furthermore, the user can now estimate the beamwidth of the vertical, far-field beam pattern $\Delta\psi = 35.93°$ and the required beam-steer angle $\psi' = 41.45°$.

Another design example would be the following. Suppose a designer who wants to manufacture a SLS that cannot do beam-steer beyond the angle of 35° due to a mechanical limitation but still wants to achieve a *SW* equal to 450 m at a height of approximately 50 m, so that $\frac{SW}{h} \approx 9$. Also, he wants the width of the one-sided blind zone equal to 5 m so that $\frac{x_{\min}}{h} = 0.1$. By looking at Tables 9 through 12, the designer finds that a SLS that will satisfy the mechanical limitation can be achieved with $\frac{\lambda}{L_y} = 1$. Consequently, the designer has to choose an operating frequency and a size in the *Y* direction of the SLS to produce a ratio $\frac{\lambda}{L_y} = 1$. A possible result could be an operating frequency of 15 kHz and $L_y = 0.1$ m. The designer can also estimate from Table 8 the 3-dB beamwidth of the vertical, far-field beam pattern $\Delta\psi = 78.0296°$.

I. HORIZONTAL BEAMWIDTH $\Delta\theta$ VERSUS $\frac{\Delta z_{\min}}{x_{\min}}$

In our attempt to analyze the performance of a SLS, we will evaluate at this point the 3-dB beamwidth of the horizontal, far-field beam pattern $\Delta\theta$, versus the ratio of the along-track resolution at the beginning of the swath width $\Delta z_{\min}$, over the width of the one-sided blind zone $x_{\min}$. This plot will help indicate the relationship between the horizontal beam pattern and the along-track resolution capabilities of a SLS.

The 3-dB beamwidth in degrees of the horizontal, far-field beam pattern $\Delta\theta$, is given by (2.13) as a function of the ratio $\frac{\Delta z_{\min}}{x_{\min}}$. Figure 21 is a plot of $\Delta\theta$ versus $\frac{\Delta z_{\min}}{x_{\min}}$ and the data used in the figure is in Table 13 in the Appendix. The range of values used for the ratio $\frac{\Delta z_{\min}}{x_{\min}}$ is between 0 and 0.2, which are considered to be typical values found in the literature ([7], [10]), with a step-size of 0.01 (1%).

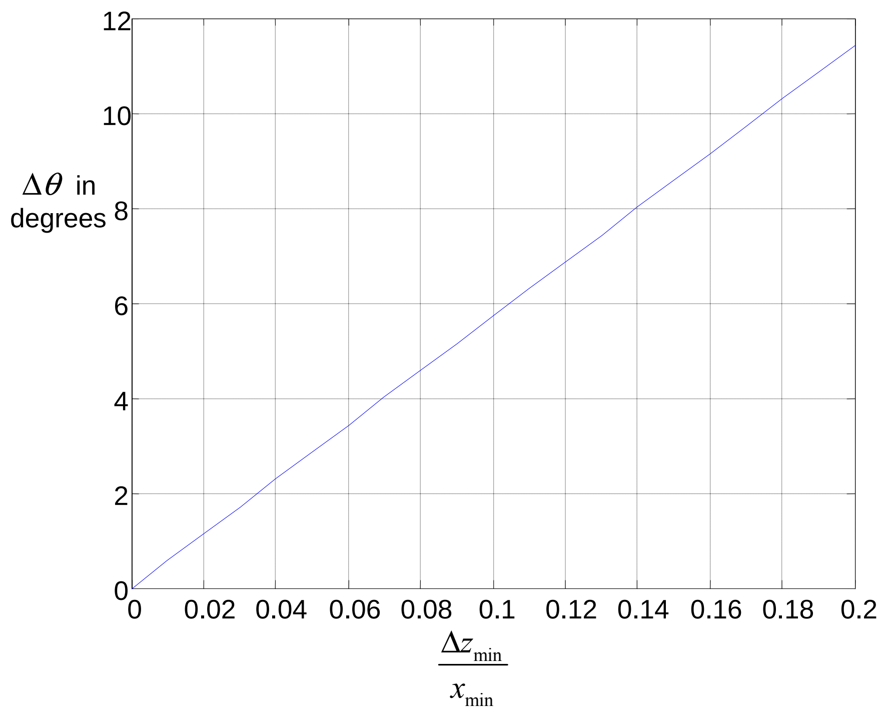

Figure 21. Three-dB beamwidth of the horizontal, far-field beam pattern $\Delta\theta$, in degrees versus $\frac{\Delta z_{\min}}{x_{\min}}$. The actual values can be found in the Appendix in Table 13.

J. ANALYSIS

Figure 21 shows that as the horizontal beamwidth $\Delta\theta$ increases, the ratio $\frac{\Delta z_{\min}}{x_{\min}}$ increases too. This relationship indicates that as $\Delta\theta$ increases, the actual capability of a SLS to discriminate small objects on the ocean floor diminishes. For example, if $x_{\min}$ is constant, then as $\Delta\theta$ increases, $\Delta z_{\min}$ increases, which means poorer along-track resolution. This result, though reasonable and expected, does not meet the needs and the requirements of today's users who try to locate small objects on the ocean floor or want to construct a high definition sea-floor map. It is obvious that as $\Delta z_{\min}$ increases, the more objects will remain unidentified on the ocean floor because of their smaller dimensions.

Figure 21 and its corresponding Table 13 can be used by a SLS user or designer who wants to find what the horizontal beamwidth should be in order for a SLS to achieve a specific along-track resolution at a particular value for the width of the one-sided blind zone. A numerical example would be as follows: suppose a designer wants to achieve an along-track resolution $\Delta z_{\min}$, equal to 0.0254 m (1 inch) for a width of the one-sided blind zone $x_{\min}$, equal to approximately 1.27 m, so that $\frac{\Delta z_{\min}}{x_{\min}} \approx 0.02$. By looking in Table 13, the designer finds out that a horizontal beamwidth $\Delta\theta$, of 1.1459° will be required to satisfy the previously mentioned ratio.

K. RATIO $\frac{\lambda}{L_z}$ VERSUS $\frac{\Delta z_{\min}}{x_{\min}}$

Finally we present a plot of the ratio of the wavelength λ, over the aperture length in the *Z* direction L_z, versus the ratio of the along-track resolution $\Delta z_{\min}$ at the beginning of the swath width $x_{\min}$, over the width of the one-sided blind zone $x_{\min}$. This plot is another approach to studying the performance of a SLS in the *XZ* plane and can help demonstrate the relationship between the aperture's length in the *Z* direction and the along-track resolution.

The ratio $\frac{\lambda}{L_z}$ versus $\frac{\Delta z_{\min}}{x_{\min}}$ is given by (2.13) and (2.17) after some algebraic manipulation. Figure 22 is a plot of $\frac{\lambda}{L_z}$ versus $\frac{\Delta z_{\min}}{x_{\min}}$ and the data used in the figure is in Table 14 in the Appendix. The range of values used for the ratio $\frac{\Delta z_{\min}}{x_{\min}}$ is between 0 and 0.2, which are considered to be typical values found in the literature ([7], [10]), with a step-size of 0.01 (1%).

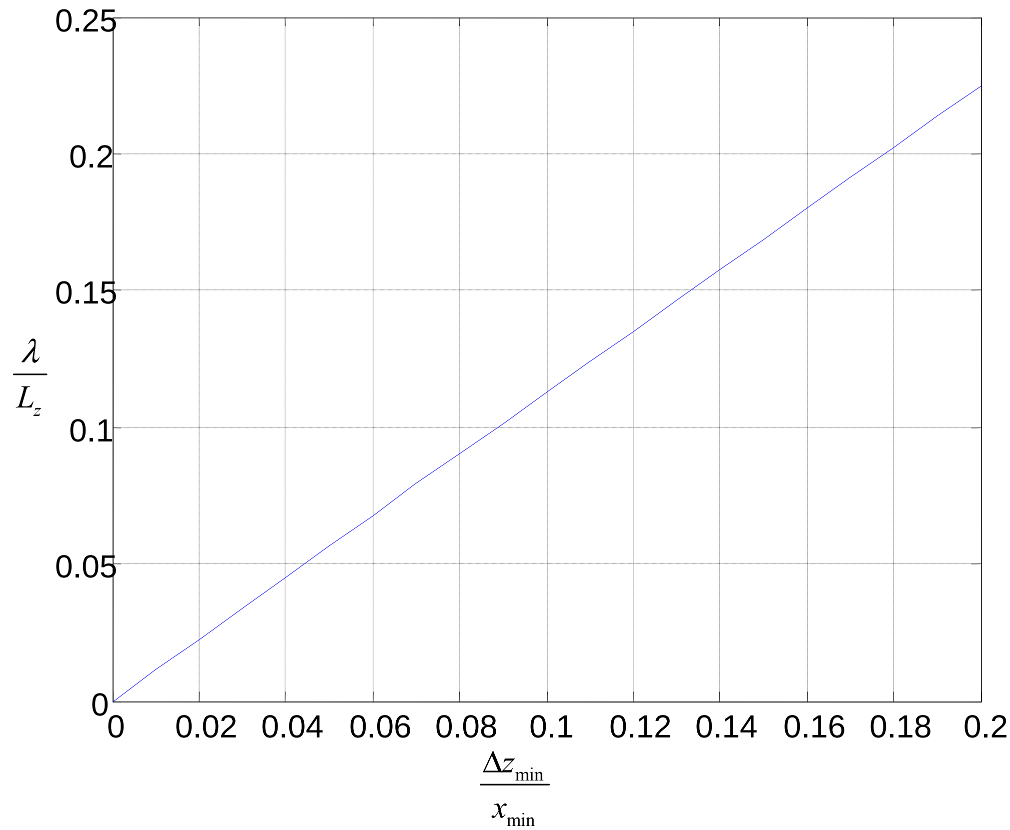

Figure 22. Ratio $\frac{\lambda}{L_z}$ versus $\frac{\Delta z_{\min}}{x_{\min}}$. The actual values can be found in the Appendix in Table 14.

L. ANALYSIS

Figure 22 shows that, as the ratio $\frac{\Delta z_{\min}}{x_{\min}}$ increases (from 0 to 0.2), the ratio $\frac{\lambda}{L_z}$ increases too. For example, from Figure 22 (and Table 14), when $\frac{\Delta z_{\min}}{x_{\min}} = 0.02$, then $\frac{\lambda}{L_z} = 0.0226$; and when $\frac{\Delta z_{\min}}{x_{\min}} = 0.1$, then $\frac{\lambda}{L_z} = 0.1127$. This result actually indicates that there is a counter proportionality between the along-track resolution capability of a SLS and its length in the *Z* direction for a fixed operational frequency and width of the one-sided blind zone. To be more precise, it is shown in Figure 22 that the smaller the object we want a SLS to identify on the ocean bottom, the bigger its size in the *Z* direction should be, if the operational frequency and the width of the one-sided blind zone remain unchanged.

An example of how Figure 22 (and its corresponding Table 14) can be used for design purposes would be as follows. If a designer wants a SLS to have an along-track resolution of 0.0254 m (1 inch) at the beginning of the swath width and width of the one-sided blind zone $x_{\min}$, equal to approximately 0,127 m, so that $\frac{\Delta z_{\min}}{x_{\min}} \approx 0.2$, then from Table 14 it can be seen that $\frac{\lambda}{L_z} \approx 0.2246$. If the operational frequency is equal to 30 kHz, so that $\lambda = 0.05$, then the length of a SLS in the *Z* direction can be computed to be equal to approximately 0.222 m.

M. OVERALL NUMERICAL EXAMPLE

Having presented Figures 6 through 22 and their corresponding Tables 1 through 14, we can at this point present an overall numerical example where by using the above mentioned figures and tables, many of the parameters of a SLS can be determined. For example, if we have an already manufactured SLS with known length in the *Y* and *Z* directions, L_y and L_z respectively, as well as the operating frequency *f*, then we can estimate the *SW*, the vertical beamwidth $\Delta\psi$, and the vertical beam-steer angle ψ', for a given height h, and width of the one-sided blind zone $x_{\min}$. We can also estimate the

along-track resolution $\Delta z_{\min}$, at the beginning of swath width $x_{\min}$ as well as the horizontal beamwidth $\Delta\theta$. A numerical example of such a scenario would be a SLS with $L_y = 0.2$ m, $L_z = 0.3$ m and $f = 30$ kHz, so that $\lambda = 0.05$ m and $\frac{\lambda}{L_y} = 0.25$. If the SLS is operated at an altitude $h = 50$ m with $x_{\min} = 10$ m, so that $\frac{x_{\min}}{h} = 0.2$, then using Table 1 we find $\frac{SW}{h} = 0.6576$, so that $SW = 32.88$ m. Furthermore, we find $\Delta\psi = 29.3068°$ and $\psi' = 60.439°$ from Tables 5 and 9, respectively. Additionally, since $\frac{\lambda}{L_z} \approx 0.167$, then using Table 14 we find $\frac{\Delta z_{\min}}{x_{\min}} \approx 0.15$, so that $\Delta z_{\min} \approx 1.5$ m, and using Table 13, we find $\Delta\theta \approx 8.578°$. Generally speaking, a way to increase the *SW* would be to decrease the operating frequency because then $\frac{\lambda}{L_y}$ would increase too, and as we stated in the previous analysis, that fact tends to increase *SW*. However, $\frac{\lambda}{L_z}$ would also increase and that would lead to an increase of the value of $\Delta z_{\min}$, resulting in a decrease in the discrimination capabilities of a SLS, an undesired side-effect. By observing Figures 6 through 22, and their corresponding Tables 1 through 14, the trade offs of the various numerical manipulations of the parameters of a SLS can become obvious and it is up to the user or designer to decide how and what should change in order to achieve the desirable results.

N. CHAPTER SUMMARY

In this chapter, plots of the characteristic parameters of a SLS were presented, mostly in the form of ratios so that it will be easier for the user or designer to decide how the desired ratios will be achieved (there will be at least two ways for the ratios to be implemented). Furthermore, numerical examples were also presented in order to emphasize the various trade offs that exist in the numerical manipulations of the values of the parameters of a SLS. Next, in Chapter IV we will discuss the shallow water

environment as an aspect of the near-field region where the previously mentioned equations do not apply. Additionally, we will suggest certain solutions and possible scenarios.

IV. NEAR-FIELD OPERATION

In this chapter, the operation of a SLS in the near-field region is examined, which is a possible situation especially when the SLS operates in shallow water environments.

A. SHALLOW WATER ENVIRONMENT

Although the term 'shallow water' is not universally defined in terms of maximum ocean depth, it is generally thought of as being less than 100 m in depth. However, for our purposes, we will consider as shallow water environments those with depths up to 40 feet (12.2 meters); depths greater than this are considered to be deep water [11].

B. NEAR-FIELD (FRESNEL) REGION

When a SLS is required to operate in a shallow water environment, it is possible that the far-field region requirements given by (2.14) and (2.16) will not be satisfied. In that case, the user will have to use the SLS in the near-field region. In such a case, all the equations mentioned in the previous chapters are invalid since they are based on operating a SLS in the far-field. Furthermore, a SLS (planar array) operating in the near-field (Fresnel) region will form a directivity function (beam pattern) D that obeys the following equation [12]:

$$D(f,r,f_y,f_z) = \sum_{m=-M'}^{M'} \sum_{n=-N'}^{N'} a_{m,n}(f) \exp\left\{ -jk \frac{\left[(md_z)^2 + (nd_y)^2 \right]}{2} \left(\frac{1}{r} - \frac{1}{r'} \right) \right\} \times$$

$$\exp\left\{ j2\pi \left[(f_z - f_z')md_z + (f_y - f_y')nd_y \right] \right\} \qquad (4.1)$$

where f is the operating frequency in Hertz, r is the slant range in meters, f_y and f_z are the spatial frequencies in the Y and Z directions in cycles per meter and are given by

$$f_y = \frac{v}{\lambda} = \frac{\sin\theta \sin\psi}{\lambda} \tag{4.2}$$

and

$$f_z = \frac{w}{\lambda} = \frac{\cos\theta}{\lambda} \tag{4.3}$$

respectively, M and N are the odd number of point elements in the Z and Y directions, respectively, that compose the planar array and determine M' and N' as follows

$$M' = \frac{M-1}{2} \tag{4.4}$$

and

$$N' = \frac{N-1}{2}, \tag{4.5}$$

$a_{m,n}(f)$ are the amplitude weights of the point elements, k is the wave number given by

$$k = \frac{2\pi f}{c} = \frac{2\pi}{\lambda}, \tag{4.6}$$

d_z and d_y are the inter element spacings in meters in the Z and Y directions, respectively, r' is the near-field range in meters for which (4.1) is being focused and finally, f_y' and f_z' are the spatial frequencies where (4.1) is being steered and are also given by (4.2) and (4.3) when you replace the angles θ and ψ with θ' and ψ', respectively.

In the case of a planar aperture lying in the *YZ* plane (see Figure 1), which is our model for a SLS, the vertical beam pattern lies in the *XY* plane where $\theta = 90°$. Therefore, the beam-steer angle $\theta' = 90°$, so that $\cos\theta = 0$ and $\cos\theta' = 0$. Furthermore, if we use rectangular amplitude weights, then $a_{m,n}(f) = 1$. With those simplifications in mind we present an example of a beam pattern in the near-field region in polar and Cartesian coordinates without doing any focusing (see Figures 23 and 24, respectively).

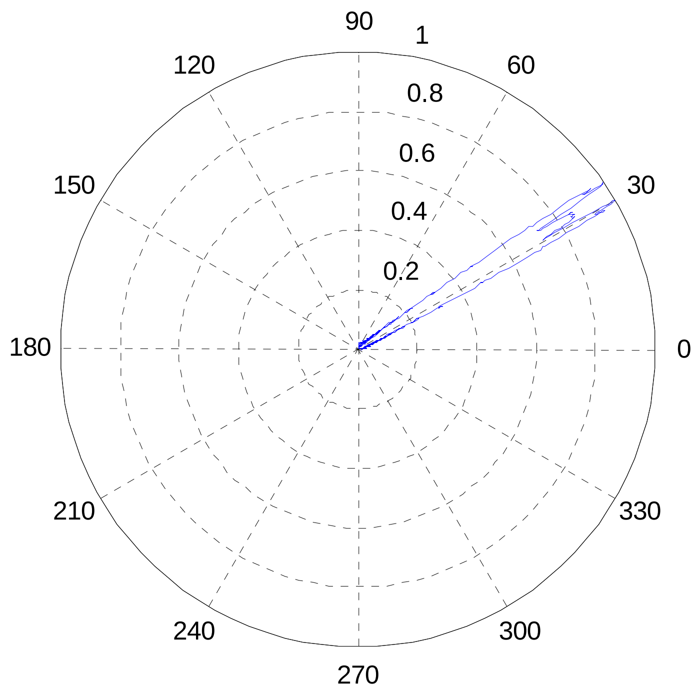

Figure 23. Polar plot of the magnitude of the normalized vertical, near-field beam pattern of an array versus ψ with $M = 101$, $N = 5$, $f = 30000$ Hz, $r = 40$ m, $d_y = d_z = 0.025$ m, $L_y = 0.1$ m, $L_z = 2.5$ m and $\psi' = 32°$.

Figure 23 and Figure 24 depict a near-field beam pattern (directivity function) with no focusing. This means that the term $\frac{1}{r'}$ in (4.1) has been deliberately neglected. Later we will present a case where we want to focus the beam pattern of the same aperture at a range r' less than $r_{NF/FF}$.

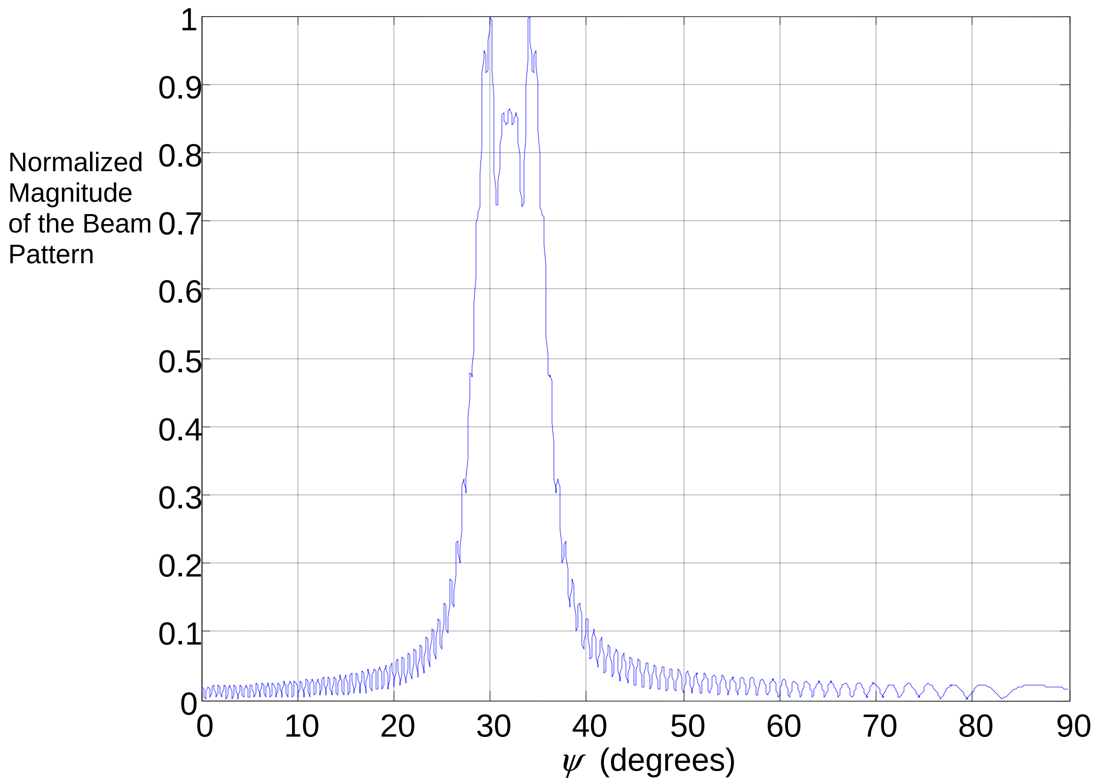

Figure 24. Cartesian plot of the magnitude of the normalized vertical, near-field beam pattern of an array versus ψ with $M = 101$, $N = 5$, $f = 30000$ Hz, $r = 40$ m, $d_y = d_z = 0.025$ m, $L_y = 0.1$ m, $L_z = 2.5$ m and $\psi' = 32°$.

C. ANALYSIS OF FIGURES 23 AND 24

In Figures 23 and 24 we presented the magnitude of the normalized vertical near-field beam pattern of an array. Such a beam pattern can be considered a typical beam

pattern in a near-field situation. Indeed it can be shown that the aperture in the example operates in the near-field region since the distance 40 m < $\pi \frac{L_y^2 + L_z^2}{4\lambda} \cong 98.33\,\text{m}$, so (2.14) is not satisfied. The following comments can be made by observing Figures 23 and 24.

The near-field beam pattern does not have a clearly defined main lobe. As can be seen in Figures 23 and 24, the beam pattern has two lobes with magnitude 1 at two different angles (at 30° and 34°). This result makes it difficult for a user to estimate what is the actual value of ψ associated with an object since its echo could have entered into either of the two lobes.

Moreover, we can observe two smaller lobes (magnitude 0.95) at angles of 29.5° and 34.5°, respectively. These smaller lobes contribute to the "angular" confusion. Apart from that, we can also observe that although the beam was steered to an angle of ψ'= 32°, the normalized magnitude of the beam pattern was not 1 in that direction. It was only 0.86.

D. NEAR-FIELD STEERED AND FOCUSED BEAM PATTERNS

In the case where we want to steer and focus a beam pattern in the near-field region, we use (4.1) but this time we do not neglect the term $\frac{1}{r'}$ where r' represents the near-field range for which we wish (4.1) to be focused. Figures 25 and 26 show in polar and Cartesian coordinates, respectively, the magnitude of the normalized vertical beam pattern of the exact same array that was used for Figures 23 and 24 versus ψ, but this time the array is focused at a near-field distance, $r' = 40\,\text{m}$. It is shown in Figures 25 and 26 that now there is only one main lobe with magnitude 1 at angle 32°, which is something actually desired, and also that the side-lobes are quite compressed since their maximum magnitudes are only 0.22.

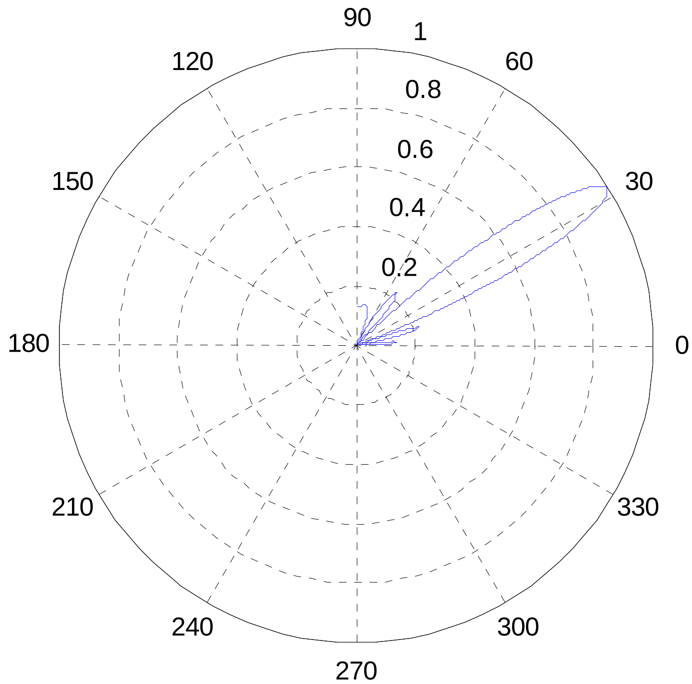

Figure 25. Polar plot of the magnitude of the normalized vertical, near-field beam pattern of an array versus ψ focused at $r' = 40$ m with $M = 101$, $N = 5$, $f = 30000$ Hz, $r = 40$ m, $d_y = d_z = 0.025$ m, $L_y = 0.1$ m, $L_z = 2.5$ m and $\psi' = 32°$.

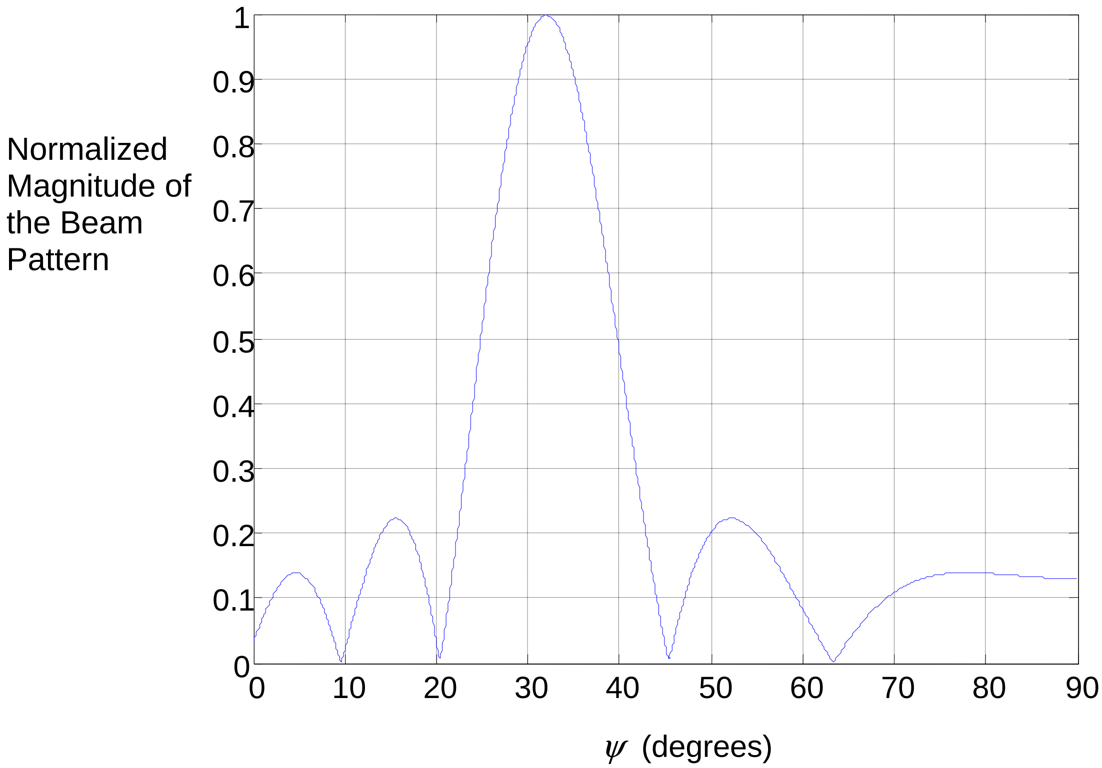

Figure 26. Cartesian plot of the magnitude of the normalized vertical, near-field beam pattern of an array versus ψ focused at $r' = 40$ m, with $M = 101$, $N = 5$, $f = 30000$ Hz, $r = 40$ m, $d_y = d_z = 0.025$ m, $L_y = 0.1$ m, $L_z = 2.5$ m and $\psi' = 32°$.

E. OPERATIONAL SCENARIOS

At this point we will present two scenarios where a value of a certain parameter of a SLS can be chosen so that a near-field situation can be avoided. The first scenario is taking as granted the sizes of a SLS, L_y and L_z, as well as the operating frequency f, and the along-track resolution at the beginning of the swath width $\Delta z_{\min}$, so it requires the user to choose an altitude h so that a near-field situation can be avoided. Although it is understood that in a shallow water environment the freedom of choosing altitudes h, will be limited, still it is possible that there will be occasions where the user will be able to avoid near-field situations by choosing an appropriate altitude. The second scenario is considering as fixed the values of the altitude h, the width of the one-sided blind zone $x_{\min}$, the operating frequency f, and the along-track resolution at the beginning of the

swath width $\Delta z_{\min}$, and allows a designer to choose the aperture's length in the Z direction so that a near-field situation can be avoided.

1. Shallow Water Scenario 1

Tabulated Case Summary

Parameters with given values	Parameters with resulting fixed values
L_y, L_z and f	$r_{NF/FF}$ and $\Delta\theta$
$\Delta z_{\min}$ and $\Delta\theta$	$x_{\min}$
$x_{\min}$ [and h chosen to avoid NF situation]	$r_{\min}$ $r_{\min} > r_{NF/FF}$ in order to have far-field situation

This scenario is considered typical for the case of an already manufactured SLS where its length in the Y and Z directions are fixed and the operating frequency f is also given. Since L_y, L_z and f are given, the range to the near-field/far-field boundary $r_{NF/FF}$ can be computed by using [see (2.14)]

$$r_{NF/FF} = \pi \frac{L_y^2 + L_z^2}{4\lambda}, \tag{4.7}$$

and the beamwidth $\Delta\theta$ is given by (2.11) and (2.12).

Having computed $\Delta\theta$, and since $\Delta z_{\min}$ is considered known, we can use (2.13) and with the proper algebraic manipulation we obtain

$$x_{\min} = \frac{\Delta z_{\min}}{2\tan\left(\frac{\Delta\theta}{2}\right)}. \tag{4.8}$$

Since $x_{\min}$ is now known, we can choose an altitude h such that

$$r_{\min} = \sqrt{h^2 + x_{\min}^2} \tag{4.9}$$

satisfies the inequality in (2.14) so that a SLS operates in the far-field region.

2. Numerical Application

Suppose we have an already manufactured SLS with known lengths in the *Y* and *Z* directions, $L_y = 0.1$ m and $L_z = 2$ m, as well as a known operating frequency, $f = 15\ kHz$. Therefore, using (4.7), $r_{NF/FF} = \pi \frac{L_y^2 + L_z^2}{4\lambda} = 31.49$ m. Using (2.11) and (2.12), we find $\Delta\theta = 2.53°$. And if $\Delta z_{\min} = 1.3$ m, then by using (4.9), $x_{\min} = 29.34$ m. Now we have to choose an altitude h such that $r_{\min} > r_{NF/FF}$. A possible solution would be $h = 12$ m.

3. Shallow Water Scenario 2

Tabulated Case Summary

Parameters with given values	Parameters with resulting fixed values
h, $x_{\min}$ and $\Delta z_{\min}$	$r_{\min}$ and $\Delta\theta$
f and $\Delta\theta$	L_z
L_z and $r_{\min}$ [and L_y chosen to avoid NF situation]	$r_{\min} > r_{NF/FF}$ in order to have far-field situation

This scenario can be used for designing purposes since it allows a designer to choose the aperture's length in the Y direction in order to avoid a near-field situation. First, if we know the altitude h, and the width of the one-sided blind zone $x_{\min}$, we can use (2.15) to compute the minimum slant range $r_{\min}$. Then, using (2.13) and since $\Delta z_{\min}$ is considered known, we can compute the 3-dB beamwidth of the horizontal far-field beam pattern in the XZ plane $\Delta\theta$. The next step is the calculation of L_z using (2.17), since the operational frequency f is known. Finally, we have to choose a length in the Y direction L_y so that $r_{\min} > r_{NF/FF}$. In other words, L_y must satisfy (2.18).

4. Numerical Application

Suppose we want to design a SLS that will operate at an altitude $h = 5\,\text{m}$ with width of the one-sided blind zone $x_{\min} = 1\,\text{m}$, along-track resolution at the beginning of the SW $\Delta z_{\min} = 0.253$ m, and operational frequency $f = 30$ kHz. Using (2.15), we can compute the minimum slant range $r_{\min} = 5.09$ m, and using (2.13), we find the 3-dB beamwidth of the horizontal, far-field beam pattern $\Delta\theta = 14.41°$. Now we know the values of all parameters necessary to evaluate L_z. Indeed, using (2.17) we find $L_z = 0.176\,\text{m}$. Now we need to choose L_y such that $r_{NF/FF}$, which is given by (4.7), will be smaller than $r_{\min}$. A possible solution would be $L_y = 0.5\,\text{m}$ because by using (4.7), we find the range to the near-field/far-field boundary, $r_{NF/FF} = 4.41\,\text{m}$, which is smaller than $r_{\min} = 5.09$ m, so we will be operating in the far-field region of the SLS.

F. CHAPTER SUMMARY

In this chapter, first a practical definition of the swallow water environment was presented, which is considered a special case for the operation of a SLS due to the fact that in such an environment, it is quite possible that a SLS will have to operate in its near-field region. We also showed the problems arising by the operation of a SLS in its near-field region and we suggested two possible scenarios with which a user/designer of a SLS can avoid operating in the near-field region by manipulating the numerical values of some parameters of a SLS. Furthermore, we briefly discussed a method of how a SLS can produce far-field beam patterns even if it operates in its near-field region by beam

steering and array focusing. Next, in Chapter V, we describe the characteristic equation of an active sonar, since a SLS is an active sonar itself, and present a mine detection example in an attempt to simulate a real case.

THIS PAGE INTENTIONALLY LEFT BLANK

V. THE ACTIVE SONAR EQUATION

In our effort to present the overall performance analysis of a SLS, we will now deal with the active sonar equation since a SLS is an active sonar itself. Its operation as well as its performance is affected by the factors that constitute the active sonar equation.

The active sonar equation for a monostatic case is [13]:

$$SL - 2TL + TS \geq DNL + DT \; . \tag{5.1}$$

A description of each of the terms in (5.1) shall be given next.

A. SOURCE LEVEL (*SL*)

Source level (SL) is a measure of the axial output of a source. If the acoustic axis of the source has been determined and the pressure amplitude along this line is measured in the far-field where the pressure varies as $\frac{1}{r}$, then the curve of $P_{ax}(r)$ versus r can be extrapolated from large r to a position $r = 1\,\mathrm{m}$ from the source to give [14]:

$$P_{ax}(1) = \lim_{r \to 1} P_{ax}(r) . \tag{5.2}$$

Since $P_{ax}(1)$ is a peak pressure amplitude, it must be reduced to an effective value $P_e(1)$ by dividing by $\sqrt{2}$. The source level is then [14]

$$SL = 20\log\left[\frac{P_e(1)}{P_{ref}}\right] \text{ dB re } P_{ref}\,, \quad P_e(1) = \frac{P_{ax}(1)}{\sqrt{2}} \tag{5.3}$$

where the reference effective pressure P_{ref} is either $1\,\mu Pa$, 20 μPa or $1\,\mu bar$ [14]. In underwater acoustics, $P_{ref} = 1$ μPa is used.

Usually the *SL* is determined by the designer of the sonar, and in a few cases, may be selected by the operator.

B. TRANSMISSION LOSS (*TL*)

The factor $2TL$ in (5.1) is the two way transmission loss because we are referring to a monostatic case where the source and receiver are at the same location. TL in dB is defined as [15]

$$TL = 10\log\left[\frac{P(1)}{P(r)}\right] \text{ dB} \tag{5.4}$$

where $P(1)$ and $P(r)$ are the acoustic pressure amplitudes measured at distances 1m and r m from the sound source, respectively [15]. For frequencies such that the absorption coefficient a in Np / m satisfies $a \ll 0.1 Np/m$, (5.4) reduces to [15]

$$TL = 20\log r + \alpha r, \quad \alpha = 8.7a \tag{5.5}$$

where α is the absorption coefficient in dB / m.

1. Absorption Coefficient (α)

The absorption coefficient α is dependent upon the operating frequency, the salinity, the temperature, the hydrostatic pressure, the pH value, and the relaxation frequencies of boric acid and magnesium sulfate. Many formulas have been published in the literature [16] - [21] trying to estimate the value of the absorption coefficient. However, for the range of frequencies that we are interested in (below 100 kHz), and considering $pH = 8$, $S = 35$ ppt and $T = 5$ °C, the following formula will be used for the absorption coefficient α in dB/km [15]:

$$\alpha = F^2 \left\{ \frac{0.08}{0.9+F^2} + \left[\frac{30}{30+F^2} \exp\left(\frac{-Z}{6} \right) \right] + 0.0004 \right\} \tag{5.6}$$

where F is the frequency in kHz and Z is the depth in km. However, for even more accurate results there should be gathered bathymetry and bottom type information for the specific water environment in which we need to operate our sonar. There should also be measurements of the sound-speed profile.

C. TARGET STRENGTH (*TS*)

Target Strength *(TS)* is a measure in dB of the ability of the target to reflect sound back toward the receiver. *TS* is*,* in general, dependent upon the frequency of the sonar as well as the geometrical shape that the target presents in the direction from which the sound waves of the sonar are coming. Depending on the kind of target that we wish to detect, we can use a corresponding formula. For a mine detection example, we can consider the mine to be a sphere. In this case, its *TS* will be independent of its orientation. Furthermore, if the spherical target has a diameter much larger than the wavelength, then the *TS* can be considered independent of the frequency as well and is given in dB by [22]

$$TS = 10\log\left(\frac{d}{4}\right)^2 \text{ dB} \tag{5.7}$$

where d is the diameter of the spherical target in yards.

For the case of an older mine that can be modeled as a cylinder of length L meters and radius a in meters, at a wavelength of λ meters , the *TS* is given in dB by [22] and [23]

$$TS = 10\log\frac{aL^2}{2\lambda} \text{ dB.} \tag{5.8}$$

According to the specific target that is desired to be detected, there are corresponding formulas that can be used based on the geometrical shape of the target, the angle of incidence that the sound wave has relevant to the target and the size of the target relevant to the wavelength used. Therefore, it is important that the intelligence sources are accurate in their description of the targets.

D. DETECTION NOISE LEVEL (*DNL*)

Competing with the received signal is noise from a variety of sources so that the definition of *DNL* is given in dB by [13]

$$DNL=NL-DI \tag{5.9}$$

where *NL* is the combined noise level of all the possible sources of noise. *NL* can be broken into three basic categories:

a. Ambient noise (biologics, waves, seismic, shipping, weather, etc.)

b. Self-noise (cavitations, mechanical, etc.)

c. Reverberation (arises from the scattering of the emitted signal from unwanted targets)

Also, *DI* stands for directivity index and describes the ability of the receiver to discriminate against noise coming from undesired directions. For a planar array, *DI* is given in dB by [24]

$$DI = 10\log\left(m \times n\right) \tag{5.10}$$

where *mn* is the total number of point elements in the planar array, all spaced by $\frac{\lambda}{2}$.

E. DETECTION THRESHOLD (*DT*)

Detection threshold (*DT*) is the value in dB by which the left-hand side of (5.1) must exceed the *DNL* in order to achieve a certain value of probability of detection for a specified probability of false alarm [13].

F. NUMERICAL APPLICATION

Having stated the active sonar equation and briefly presented the meaning of each factor we can now present an example of mine detection using a SLS. First, we have to make an assumption about the value of *SL*. Based on reference [25], we will use $SL = 204$ dB re 1 μPa. Second, we have to estimate the TL, which is given by (5.5). Toward that end we need to specify the operating frequency *F*, the range *r* at which we wish to detect the target, and the depth *Z*, where we expect the target to be. A realistic scenario would be an operating frequency $F = 10$ kHz for a SLS, a range $r = 1000$ m and a depth $Z = 15$ m. Plugging the numbers into (5.6) yields $\alpha = 1.085$ dB/km, and since we know $r = 1000$ m, then using (5.5) yields $TL = 61.085$ dB. However, for most accurate results, reference [21] can be used provided that all parameters required are known. In our example we considered $pH = 8.5$, $S = 35\,ppt$ and $T = 5$ °C.

Concerning the TS of the mine, the estimation is based mostly on the geometrical shape of the mine as well as the angle of incidence of the sound wave relevant to the target. In real world problems, mines are usually represented as cylinders. Therefore, we can suppose a mine to be a cylinder of length $L = 2$ m with hemispherical ends of radius, $a = 0.15$ m. If the angle of incidence is normal to the beam surface of the target, then (5.8) applies and yields [23]

$$TS = 10\log\frac{0.15\times 2^2}{2\times 0.15} = 3 \text{ dB}. \tag{5.11}$$

If the target presents its end parts to the sound wave, then it is considered as a sphere with diameter $d = 2.516$ yards and (5.7) applies and yields [22]

$$TS = 10\log\left(\frac{2.516}{4}\right)^2 = -4.026 \text{ dB.} \tag{5.12}$$

The next step in our example is the estimation of *DNL*. The *DI* factor is mostly determined by the geometry used for the construction of the planar array. Since we used $F = 10$ kHz, we need a half-wavelength interelement spacing of $d_y = d_z = 0.075$ m. A possible design would be 3 lines having 27 elements each. Using (5.10) yields

$$DI = 10\log 3\times 27 = 19 \text{ dB.} \tag{5.13}$$

Concerning the *NL,* it is obvious that only estimations can be made since it is a factor that is affected by many random causes like ambient noise or reverberation. However, some charts exist that try to predict what the ambient noise will be in certain geographical areas versus the operating frequency used and for specified conditions of shipping (e.g., high shipping versus low shipping in the Strait of Malacca). That way we can predict to some degree the *NL* factor. In our example, considering that we need to detect a mine in a shallow water environment (15 m) and possibly near a harbor or other kind of naval facility, we can estimate the *NL* to be as high as 90 dB. So we can compute *DNL* using (5.9)

$$DNL = 90 - 19 = 71 \text{ dB.} \tag{5.14}$$

The final step in our example is to choose the value of *DT*. From the values that we have already computed, it seems that in order to detect the mine if its beam is presented to our SLS, we need a $DT \le 13.83$ dB. In the case where its ends are being presented, we need a $DT \le 6.804$ dB. Both cases are doable and just indicate a limit in our detection threshold that we cannot exceed if we want to have an actual detection. It would be much safer to choose the second option, $DT \le 6.804$ dB, since this choice will

guarantee to some degree the detection of the target in either of the two possible geometries that it may present to the SLS. Furthermore, with that choice we have a bigger possibility of detection.

In order to specify the exact probability of detection $P(D)$, as well as the probability of false alarm $P(FA)$, that this configuration can provide us, we need to specify the integration time, the bandwidth of our processor and the processing scheme. We also need to use Figure 27 from [26] or tables for the Gaussian distribution. Figure 27(a and b) is based on the assumption that the probability density functions of both the signal and noise are Gaussian with equal standard deviations.

For square-law processing, *DT* is given in dB by [26]

$$DT = 5\log\frac{d'^2}{\omega\tau} \tag{5.15}$$

where d' is the dimensionless detectability index, ω is the bandwidth of our processor in Hz and τ is the processing time in sec.

For example, if we want to detect the beam aspect of the target with $P(D) = 0.5$ and $P(FA) = 10^{-4}$, then from Figure 27(b) we obtain $d' = 4$. If we have $\omega = 200$ Hz and $\tau = 1$ msec, then using (5.15)

$$DT = 9.51 \text{ dB.} \tag{5.16}$$

However, it must be said that the above value of *DT* does not satisfy the situation where the end parts of the target are being presented to our SLS beam, since for that situation we would need a lower value for DT according to the active sonar equation. It is important to note that the value of *DT* depends on the type of processing that is done as well as on the desired probability of detection and false alarm that the operator is willing

to accept. It may seem reasonable to always choose very small values for DT, but on the other hand, too many false alarms may unnecessarily burden a Naval Task force.

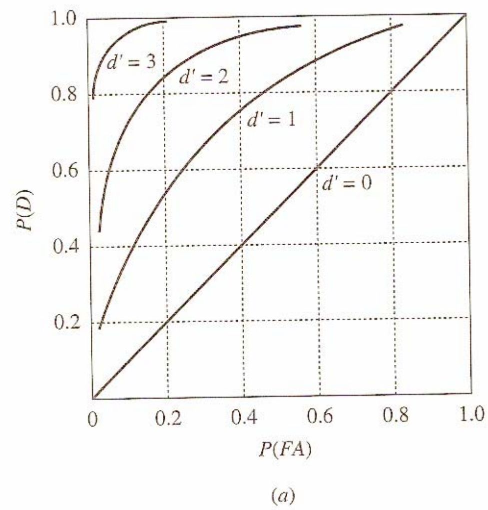

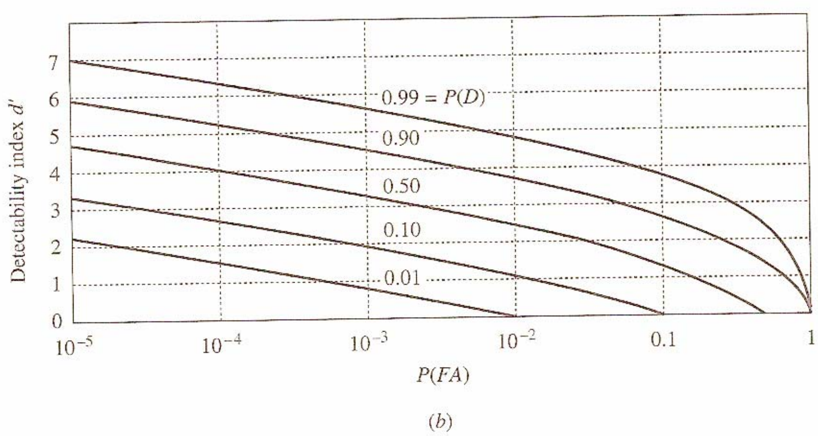

Figure 27. Receiver operating characteristic (ROC) curves, where the probability density functions for both the signal and noise are considered Gaussian with equal standard deviations (After [26])

G. CHAPTER SUMMARY

In this chapter we presented the active sonar equation and discussed its parameters as well as the various speculations that arise in the evaluation of these

parameters. We also presented an example for a SLS (planar array) problem, evaluating the active sonar equation using some reasonable and meaningful values. Next, in Chapter VI, we will present a summary with conclusions and goals achieved in this thesis and we will make suggestions for future work.

THIS PAGE INTENTIONALLY LEFT BLANK

VI CONCLUSIONS AND FUTURE WORK

A. CONCLUSIONS

This thesis examined the behavior of a SLS in various operational scenarios. First, we presented the basic parameters and formulas that rule the operation of a SLS in the far-field region. Next, we presented four graphs, and their corresponding tables, of $\frac{SW}{h}$ versus $\frac{x_{\min}}{h}$ for four different fixed values of $\frac{\lambda}{L_y}$. We analyzed the graphs and found that the *ACR* increases as the ratio $\frac{\lambda}{L_y}$ increases and also that there is a limit in our ability to use arbitrary ratios of wavelength over aperture length in the *Y* direction. Moreover, we presented numerical examples showing how these graphs can be used for a SLS experiment. Furthermore, we presented a second set of four graphs, and their corresponding tables, of $\Delta\psi$ versus $\frac{x_{\min}}{h}$ for different fixed values of $\frac{\lambda}{L_y}$. The analysis of these graphs confirmed the results we had from the first set of graphs. In order to conclude the performance analysis of the vertical, far-field beam pattern, we also presented a third set of four graphs, and their corresponding tables, of ψ' versus $\frac{x_{\min}}{h}$ for different fixed values of $\frac{\lambda}{L_y}$. We analyzed these graphs and used their tables in order to present some numerical examples that can help demonstrate how these graphs can be used by a user or designer.

Concerning the horizontal, far-field beam pattern, we presented two graphs and their corresponding tables. The first graph depicted $\Delta\theta$ versus $\frac{\Delta z_{\min}}{x_{\min}}$ and the second presented the ratio $\frac{\lambda}{L_z}$ versus $\frac{\Delta z_{\min}}{x_{\min}}$. By analyzing these two graphs, it was seen that the ratio $\frac{\Delta z_{\min}}{x_{\min}}$ increases as the 3-dB beamwidth of the horizontal far-field beam pattern $\Delta\theta$,

increases. In addition, there is a counter proportionality between the along-track resolution capability of a SLS and its length in the *Z* direction for a fixed operational frequency and width of the one-sided blind zone. We also presented numerical examples trying to explain how these graphs can be used in the real world.

The next step was to show the various problems that may arise in a near-field operation by showing a near-field beam pattern and analyzing it. A near-field operation is considered a possible situation especially when a SLS is operating in shallow water environments. Moreover we stated two possible scenarios and presented two numerical examples respectively, where a near-field operation may be avoided by manipulating the values of certain parameters of a SLS that operates in shallow waters. Finally, we described the active sonar equation, and after a brief explanation of its factors we presented a numerical example of mine detection, trying to use realistic values for all parameters involved and comment on the various speculations that in such cases, usually arise.

The key findings from this work are as follows:

- The creation of the previously mentioned graphs and their corresponding tables are considered unique in the literature and can help a user or designer to better operate or design a SLS experiment. Furthermore, because in most of our graphs we used the form of ratios, it will be easier for the user or designer to decide how the desired ratios will be achieved since there will be at least two ways for the ratios to be implemented.
- During the creation of the previous mentioned graphs, the inequality $\sin\psi' > \frac{\Delta\nu}{2}$ appearing in (2.1), posed a limit in our ability to choose high values for the ratio $\frac{\lambda}{L_y}$. Indeed for $\frac{\lambda}{L_y} > 1.128$, no plots can be made.
- We showed that there are possible scenarios that may allow a SLS that operates in shallow waters to achieve a far-field beam pattern, without using beam steering and aperture focusing.

- The overall performance of a SLS is dependent upon the parameters that constitute the active sonar equation, namely the *SL*, *TL*, *TS*, *DNL* and *DT*. Although some of them can be accurately computed (like *SL*), for other parameters, only estimates can be made based on intelligence (like *TS*) or statistical data (like *NL*). However, all of them can severely affect the performance of any active sonar.

B FUTURE WORK

This thesis was based on the assumptions that the platform of the SLS moves with a constant speed and maintains a constant altitude above the ocean bottom. It would be important to perform research in cases where the speed of the platform and the altitude are not constant. Furthermore, it would also be important to perform research, from the performance analysis point of view, in cases where the SLS is not a planar array but a curved (conformal) array and the speed of sound is not considered constant but rather a function of depth.

A separate important task would be to research various signal processing methods that may be used for beamforming for planar arrays for SLS applications. The signal processing algorithms would need to be examined from the performance point of view for various operational scenarios (far-field and near-field) with different operational goals.

THIS PAGE INTENTIONALLY LEFT BLANK

APPENDIX TABLES

In the Appendix we present all tables that correspond to the actual graphs that were displayed in Chapter III of the thesis.

Table 1. Values of $\frac{SW}{h}$ as a function of $\frac{x_{\min}}{h}$ for $\frac{\lambda}{L_y} = 0.25$ where SW is the one-sided swath width, h is the altitude, $x_{\min}$ is the width of the one-sided blind zone, λ is the wavelength, and L_y is the aperture length in the Y direction.

$\frac{x_{\min}}{h}$	$\frac{SW}{h}$	$\frac{x_{\min}}{h}$	$\frac{SW}{h}$
0	0.8062	0.1500	0.6854
0.0100	0.7964	0.1600	0.6794
0.0200	0.7867	0.1700	0.6736
0.0300	0.7774	0.1800	0.6680
0.0400	0.7683	0.1900	0.6627
0.0500	0.7595	0.2000	0.6576
0.0600	0.7509	0.2100	0.6528
0.0700	0.7426	0.2200	0.6481
0.0800	0.7346	0.2300	0.6437
0.0900	0.7268	0.2400	0.6395
0.1000	0.7193	0.2500	0.6356
0.1100	0.7120	0.2600	0.6318
0.1200	0.7050	0.2700	0.6283
0.1300	0.6982	0.2800	0.6250
0.1400	0.6917	0.2900	0.6218

$\frac{x_{\min}}{h}$	$\frac{SW}{h}$	$\frac{x_{\min}}{h}$	$\frac{SW}{h}$
0.3000	0.6189	0.5200	0.6009
0.3100	0.6162	0.5300	0.6020
0.3200	0.6137	0.5400	0.6032
0.3300	0.6114	0.5500	0.6045
0.3400	0.6092	0.5600	0.6060
0.3500	0.6073	0.5700	0.6076
0.3600	0.6056	0.5800	0.6094
0.3700	0.6040	0.5900	0.6113
0.3800	0.6026	0.6000	0.6134
0.3900	0.6014	0.6100	0.6156
0.4000	0.6004	0.6200	0.6179
0.4100	0.5995	0.6300	0.6203
0.4200	0.5988	0.6400	0.6229
0.4300	0.5983	0.6500	0.6257
0.4400	0.5980	0.6600	0.6285
0.4500	0.5978	0.6700	0.6315
0.4600	0.5978	0.6800	0.6346
0.4700	0.5979	0.6900	0.6379
0.4800	0.5982	0.7000	0.6412
0.4900	0.5986	0.7100	0.6447
0.5000	0.5992	0.7200	0.6484
0.5100	0.6000	0.7300	0.6521

$\frac{x_{\min}}{h}$	$\frac{SW}{h}$	$\frac{x_{\min}}{h}$	$\frac{SW}{h}$
0.7400	0.6560	0.9600	0.7726
0.7500	0.6600	0.9700	0.7793
0.7600	0.6641	0.9800	0.7861
0.7700	0.6684	0.9900	0.7931
0.7800	0.6728	1.0000	0.8002
0.7900	0.6773	1.0100	0.8074
0.8000	0.6819	1.0200	0.8147
0.8100	0.6866	1.0300	0.8222
0.8200	0.6915	1.0400	0.8298
0.8300	0.6965	1.0500	0.8375
0.8400	0.7016	1.0600	0.8454
0.8500	0.7069	1.0700	0.8533
0.8600	0.7122	1.0800	0.8614
0.8700	0.7177	1.0900	0.8697
0.8800	0.7233	1.1000	0.8780
0.8900	0.7290	1.1100	0.8865
0.9000	0.7349	1.1200	0.8952
0.9100	0.7409	1.1300	0.9039
0.9200	0.7470	1.1400	0.9128
0.9300	0.7532	1.1500	0.9218
0.9400	0.7595	1.1600	0.9310
0.9500	0.7660	1.1700	0.9403

$\frac{x_{\min}}{h}$	$\frac{SW}{h}$	$\frac{x_{\min}}{h}$	$\frac{SW}{h}$
1.1800	0.9497	1.4000	1.1937
1.1900	0.9593	1.4100	1.2065
1.2000	0.9690	1.4200	1.2196
1.2100	0.9789	1.4300	1.2327
1.2200	0.9888	1.4400	1.2461
1.2300	0.9990	1.4500	1.2596
1.2400	1.0092	1.4600	1.2733
1.2500	1.0197	1.4700	1.2871
1.2600	1.0302	1.4800	1.3011
1.2700	1.0409	1.4900	1.3153
1.2800	1.0518	1.5000	1.3297
1.2900	1.0628	1.5100	1.3442
1.3000	1.0739	1.5200	1.3590
1.3100	1.0852	1.5300	1.3739
1.3200	1.0966	1.5400	1.3890
1.3300	1.1082	1.5500	1.4042
1.3400	1.1200	1.5600	1.4197
1.3500	1.1319	1.5700	1.4353
1.3600	1.1439	1.5800	1.4512
1.3700	1.1561	1.5900	1.4672
1.3800	1.1685	1.6000	1.4834
1.3900	1.1810	1.6100	1.4998

$\frac{x_{\min}}{h}$	$\frac{SW}{h}$	$\frac{x_{\min}}{h}$	$\frac{SW}{h}$
1.6200	1.5164	1.8100	1.8721
1.6300	1.5332	1.8200	1.8931
1.6400	1.5502	1.8300	1.9144
1.6500	1.5674	1.8400	1.9359
1.6600	1.5848	1.8500	1.9576
1.6700	1.6025	1.8600	1.9796
1.6800	1.6203	1.8700	2.0019
1.6900	1.6383	1.8800	2.0244
1.7000	1.6566	1.8900	2.0472
1.7100	1.6751	1.9000	2.0702
1.7200	1.6937	1.9100	2.0935
1.7300	1.7126	1.9200	2.1171
1.7400	1.7318	1.9300	2.1410
1.7500	1.7511	1.9400	2.1651
1.7600	1.7707	1.9500	2.1896
1.7700	1.7905	1.9600	2.2143
1.7800	1.8106	1.9700	2.2393
1.7900	1.8309	1.9800	2.2646
1.8000	1.8514	1.9900	2.2902
		2.0000	2.3161

Table 2. Values of $\frac{SW}{h}$ as a function of $\frac{x_{min}}{h}$ for $\frac{\lambda}{L_y} = 0.5$ where SW is the one-sided swath width, h is the altitude, x_{min} is the width of the one-sided blind zone, λ is the wavelength, and L_y is the aperture length in the Y direction.

$\frac{x_{min}}{h}$	$\frac{SW}{h}$	$\frac{x_{min}}{h}$	$\frac{SW}{h}$
0	1.4910	0.1900	1.3710
0.0100	1.4812	0.2000	1.3685
0.0200	1.4718	0.2100	1.3665
0.0300	1.4628	0.2200	1.3648
0.0400	1.4542	0.2300	1.3635
0.0500	1.4459	0.2400	1.3626
0.0600	1.4380	0.2500	1.3620
0.0700	1.4306	0.2600	1.3619
0.0800	1.4235	0.2700	1.3622
0.0900	1.4168	0.2800	1.3628
0.1000	1.4104	0.2900	1.3638
0.1100	1.4045	0.3000	1.3652
0.1200	1.3990	0.3100	1.3670
0.1300	1.3938	0.3200	1.3692
0.1400	1.3890	0.3300	1.3718
0.1500	1.3847	0.3400	1.3747
0.1600	1.3807	0.3500	1.3781
0.1700	1.3771	0.3600	1.3818
0.1800	1.3738	0.3700	1.3860

$\frac{x_{\min}}{h}$	$\frac{SW}{h}$	$\frac{x_{\min}}{h}$	$\frac{SW}{h}$
0.3800	1.3905	0.6000	1.5956
0.3900	1.3955	0.6100	1.6100
0.4000	1.4008	0.6200	1.6249
0.4100	1.4065	0.6300	1.6404
0.4200	1.4127	0.6400	1.6563
0.4300	1.4192	0.6500	1.6727
0.4400	1.4262	0.6600	1.6896
0.4500	1.4336	0.6700	1.7071
0.4600	1.4413	0.6800	1.7251
0.4700	1.4495	0.6900	1.7436
0.4800	1.4581	0.7000	1.7626
0.4900	1.4672	0.7100	1.7823
0.5000	1.4766	0.7200	1.8025
0.5100	1.4865	0.7300	1.8232
0.5200	1.4969	0.7400	1.8446
0.5300	1.5076	0.7500	1.8665
0.5400	1.5188	0.7600	1.8891
0.5500	1.5305	0.7700	1.9123
0.5600	1.5426	0.7800	1.9361
0.5700	1.5551	0.7900	1.9606
0.5800	1.5681	0.8000	1.9857
0.5900	1.5816	0.8100	2.0115

$\frac{x_{min}}{h}$	$\frac{SW}{h}$	$\frac{x_{min}}{h}$	$\frac{SW}{h}$
0.8200	2.0379	1.0400	2.8312
0.8300	2.0651	1.0500	2.8790
0.8400	2.0930	1.0600	2.9280
0.8500	2.1216	1.0700	2.9784
0.8600	2.1510	1.0800	3.0301
0.8700	2.1812	1.0900	3.0831
0.8800	2.2121	1.1000	3.1376
0.8900	2.2438	1.1100	3.1936
0.9000	2.2764	1.1200	3.2511
0.9100	2.3098	1.1300	3.3101
0.9200	2.3440	1.1400	3.3707
0.9300	2.3792	1.1500	3.4331
0.9400	2.4152	1.1600	3.4971
0.9500	2.4522	1.1700	3.5630
0.9600	2.4901	1.1800	3.6306
0.9700	2.5290	1.1900	3.7002
0.9800	2.5689	1.2000	3.7718
0.9900	2.6099	1.2100	3.8455
1.0000	2.6519	1.2200	3.9212
1.0100	2.6950	1.2300	3.9992
1.0200	2.7392	1.2400	4.0795
1.0300	2.7846	1.2500	4.1621

$\frac{x_{\min}}{h}$	$\frac{SW}{h}$	$\frac{x_{\min}}{h}$	$\frac{SW}{h}$
1.2600	4.2472	1.4800	7.0188
1.2700	4.3349	1.4900	7.2039
1.2800	4.4253	1.5000	7.3965
1.2900	4.5184	1.5100	7.5970
1.3000	4.6145	1.5200	7.8060
1.3100	4.7135	1.5300	8.0238
1.3200	4.8157	1.5400	8.2511
1.3300	4.9212	1.5500	8.4884
1.3400	5.0301	1.5600	8.7364
1.3500	5.1426	1.5700	8.9959
1.3600	5.2588	1.5800	9.2675
1.3700	5.3789	1.5900	9.5522
1.3800	5.5030	1.6000	9.8508
1.3900	5.6315	1.6100	10.1644
1.4000	5.7644	1.6200	10.4940
1.4100	5.9021	1.6300	10.8409
1.4200	6.0446	1.6400	11.2065
1.4300	6.1924	1.6500	11.5922
1.4400	6.3456	1.6600	11.9997
1.4500	6.5045	1.6700	12.4308
1.4600	6.6695	1.6800	12.8877
1.4700	6.8408	1.6900	13.3726

$\frac{x_{\min}}{h}$	$\frac{SW}{h}$	$\frac{x_{\min}}{h}$	$\frac{SW}{h}$
1.7000	13.8880	1.8500	28.8868
1.7100	14.4371	1.8600	30.8741
1.7200	15.0229	1.8700	33.1212
1.7300	15.6494	1.8800	35.6824
1.7400	16.3208	1.8900	38.6281
1.7500	17.0420	1.9000	42.0516
1.7600	17.8187	1.9100	46.0788
1.7700	18.6575	1.9200	50.8844
1.7800	19.5659	1.9300	56.7174
1.7900	20.5530	1.9400	63.9458
1.8000	21.6292	1.9500	73.1373
1.8100	22.8071	1.9600	85.2156
1.8200	24.1017	1.9700	101.7920
1.8300	25.5310	1.9800	125.9507
1.8400	27.1171	1.9900	164.4315
		2.0000	235.3249

Table 3. Values of $\frac{SW}{h}$ as a function of $\frac{x_{\min}}{h}$ for $\frac{\lambda}{L_y} = 0.75$ where SW is the one-sided swath width, h is the altitude, $x_{\min}$ is the width of the one-sided blind zone, λ is the wavelength, and L_y is the aperture length in the Y direction.

$\frac{x_{\min}}{h}$	$\frac{SW}{h}$	$\frac{x_{\min}}{h}$	$\frac{SW}{h}$
0	2.8079	0.1800	2.7839
0.0100	2.7983	0.1900	2.7922
0.0200	2.7898	0.2000	2.8016
0.0300	2.7821	0.2100	2.8120
0.0400	2.7754	0.2200	2.8236
0.0500	2.7697	0.2300	2.8363
0.0600	2.7649	0.2400	2.8502
0.0700	2.7610	0.2500	2.8652
0.0800	2.7582	0.2600	2.8815
0.0900	2.7563	0.2700	2.8990
0.1000	2.7553	0.2800	2.9178
0.1100	2.7554	0.2900	2.9378
0.1200	2.7564	0.3000	2.9592
0.1300	2.7584	0.3100	2.9819
0.1400	2.7615	0.3200	3.0061
0.1500	2.7655	0.3300	3.0316
0.1600	2.7706	0.3400	3.0586
0.1700	2.7768	0.3500	3.0871

$\frac{x_{\min}}{h}$	$\frac{SW}{h}$	$\frac{x_{\min}}{h}$	$\frac{SW}{h}$
0.3600	3.1172	0.5800	4.3055
0.3700	3.1488	0.5900	4.3927
0.3800	3.1821	0.6000	4.4841
0.3900	3.2171	0.6100	4.5798
0.4000	3.2538	0.6200	4.6802
0.4100	3.2924	0.6300	4.7853
0.4200	3.3328	0.6400	4.8956
0.4300	3.3752	0.6500	5.0113
0.4400	3.4196	0.6600	5.1329
0.4500	3.4660	0.6700	5.2606
0.4600	3.5147	0.6800	5.3949
0.4700	3.5655	0.6900	5.5362
0.4800	3.6188	0.7000	5.6850
0.4900	3.6745	0.7100	5.8418
0.5000	3.7327	0.7200	6.0072
0.5100	3.7936	0.7300	6.1819
0.5200	3.8572	0.7400	6.3666
0.5300	3.9238	0.7500	6.5620
0.5400	3.9934	0.7600	6.7691
0.5500	4.0662	0.7700	6.9888
0.5600	4.1424	0.7800	7.2221
0.5700	4.2221	0.7900	7.4704

$\frac{x_{\min}}{h}$	$\frac{SW}{h}$	$\frac{x_{\min}}{h}$	$\frac{SW}{h}$
0.8000	7.7350	0.9600	16.5901
0.8100	8.0174	0.9700	17.7680
0.8200	8.3194	0.9800	19.1107
0.8300	8.6429	0.9900	20.6549
0.8400	8.9902	1.0000	22.4491
0.8500	9.3640	1.0100	24.5589
0.8600	9.7671	1.0200	27.0747
0.8700	10.2031	1.0300	30.1252
0.8800	10.6759	1.0400	33.9001
0.8900	11.1903	1.0500	38.6907
0.9000	11.7518	1.0600	44.9687
0.9100	12.3670	1.0700	53.5517
0.9200	13.0438	1.0800	65.9905
0.9300	13.7915	1.0900	85.6293
0.9400	14.6218	1.1000	121.2531
0.9500	15.5488	1.1100	205.7365
		1.1200	658.6102

Table 4. Values of $\frac{SW}{h}$ as a function of $\frac{x_{\min}}{h}$ for $\frac{\lambda}{L_y}=1$ where SW is the one-sided swath width, h is the altitude, $x_{\min}$ is the width of the one-sided blind zone, λ is the wavelength, and L_y is the aperture length in the Y direction.

$\frac{x_{\min}}{h}$	$\frac{SW}{h}$	$\frac{x_{\min}}{h}$	$\frac{SW}{h}$
0	8.7147	0.1800	9.9558
0.0100	8.7086	0.1900	10.1325
0.0200	8.7103	0.2000	10.3256
0.0300	8.7197	0.2100	10.5365
0.0400	8.7371	0.2200	10.7667
0.0500	8.7624	0.2300	11.0180
0.0600	8.7960	0.2400	11.2925
0.0700	8.8379	0.2500	11.5925
0.0800	8.8884	0.2600	11.9206
0.0900	8.9479	0.2700	12.2801
0.1000	9.0165	0.2800	12.6745
0.1100	9.0947	0.2900	13.1083
0.1200	9.1830	0.3000	13.5865
0.1300	9.2817	0.3100	14.1152
0.1400	9.3916	0.3200	14.7015
0.1500	9.5131	0.3300	15.3543
0.1600	9.6471	0.3400	16.0843
0.1700	9.7944	0.3500	16.9046

$\frac{x_{\min}}{h}$	$\frac{SW}{h}$	$\frac{x_{\min}}{h}$	$\frac{SW}{h}$
0.3600	17.8316	0.4400	33.6575
0.3700	18.8861	0.4500	38.1150
0.3800	20.0943	0.4600	43.9921
0.3900	21.4908	0.4700	52.0865
0.4000	23.1211	0.4800	63.9325
0.4100	25.0468	0.4900	82.9047
0.4200	27.3536	0.5000	118.1593
0.4300	30.1635	0.5100	206.2933
		0.5200	821.3063

Table 5. Values of $\Delta\psi$ as a function of $\frac{x_{\min}}{h}$ for $\frac{\lambda}{L_y} = 0.25$ where $\Delta\psi$ is the 3-dB beamwidth of the vertical, far-field beam pattern, h is the altitude, $x_{\min}$ is the width of the one-sided blind zone, λ is the wavelength, and L_y is the aperture length in the Y direction.

$\frac{x_{\min}}{h}$	$\Delta\psi$ (deg)	$\frac{x_{\min}}{h}$	$\Delta\psi$ (deg)
0	38.8766	0.1700	30.5022
0.0100	38.3082	0.1800	30.0947
0.0200	37.7490	0.1900	29.6963
0.0300	37.1992	0.2000	29.3068
0.0400	36.6588	0.2100	28.9263
0.0500	36.1279	0.2200	28.5546
0.0600	35.6065	0.2300	28.1915
0.0700	35.0947	0.2400	27.8370
0.0800	34.5925	0.2500	27.4908
0.0900	34.0998	0.2600	27.1530
0.1000	33.6168	0.2700	26.8232
0.1100	33.1434	0.2800	26.5015
0.1200	32.6795	0.2900	26.1876
0.1300	32.2252	0.3000	25.8814
0.1400	31.7804	0.3100	25.5827
0.1500	31.3450	0.3200	25.2914
0.1600	30.9190	0.3300	25.0074

$\frac{x_{min}}{h}$	$\Delta\psi$ (deg)	$\frac{x_{min}}{h}$	$\Delta\psi$ (deg)
0.3400	24.7304	0.5500	20.2911
0.3500	24.4604	0.5600	20.1337
0.3600	24.1972	0.5700	19.9802
0.3700	23.9406	0.5800	19.8306
0.3800	23.6905	0.5900	19.6848
0.3900	23.4467	0.6000	19.5426
0.4000	23.2091	0.6100	19.4039
0.4100	22.9776	0.6200	19.2687
0.4200	22.7519	0.6300	19.1369
0.4300	22.5320	0.6400	19.0083
0.4400	22.3176	0.6500	18.8828
0.4500	22.1088	0.6600	18.7605
0.4600	21.9052	0.6700	18.6412
0.4700	21.7069	0.6800	18.5248
0.4800	21.5135	0.6900	18.4112
0.4900	21.3252	0.7000	18.3003
0.5000	21.1416	0.7100	18.1922
0.5100	20.9626	0.7200	18.0867
0.5200	20.7882	0.7300	17.9837
0.5300	20.6183	0.7400	17.8831
0.5400	20.4526	0.7500	17.7850

$\frac{x_{\min}}{h}$	$\Delta\psi$ (deg)	$\frac{x_{\min}}{h}$	$\Delta\psi$ (deg)
0.7600	17.6892	0.9700	16.1175
0.7700	17.5956	0.9800	16.0597
0.7800	17.5043	0.9900	16.0031
0.7900	17.4151	1.0000	15.9478
0.8000	17.3280	1.0100	15.8936
0.8100	17.2430	1.0200	15.8406
0.8200	17.1599	1.0300	15.7887
0.8300	17.0787	1.0400	15.7379
0.8400	16.9994	1.0500	15.6882
0.8500	16.9219	1.0600	15.6395
0.8600	16.8462	1.0700	15.5919
0.8700	16.7722	1.0800	15.5452
0.8800	16.6999	1.0900	15.4995
0.8900	16.6292	1.1000	15.4547
0.9000	16.5601	1.1100	15.4109
0.9100	16.4926	1.1200	15.3679
0.9200	16.4265	1.1300	15.3259
0.9300	16.3619	1.1400	15.2846
0.9400	16.2988	1.1500	15.2442
0.9500	16.2370	1.1600	15.2046
0.9600	16.1766	1.1700	15.1659

$\frac{x_{\min}}{h}$	$\Delta\psi$ (deg)	$\frac{x_{\min}}{h}$	$\Delta\psi$ (deg)
1.1800	15.1278	1.3900	14.4785
1.1900	15.0906	1.4000	14.4536
1.2000	15.0540	1.4100	14.4290
1.2100	15.0182	1.4200	14.4049
1.2200	14.9831	1.4300	14.3813
1.2300	14.9486	1.4400	14.3580
1.2400	14.9149	1.4500	14.3352
1.2500	14.8817	1.4600	14.3128
1.2600	14.8493	1.4700	14.2908
1.2700	14.8174	1.4800	14.2691
1.2800	14.7861	1.4900	14.2478
1.2900	14.7555	1.5000	14.2269
1.3000	14.7254	1.5100	14.2064
1.3100	14.6959	1.5200	14.1862
1.3200	14.6669	1.5300	14.1664
1.3300	14.6385	1.5400	14.1469
1.3400	14.6106	1.5500	14.1277
1.3500	14.5832	1.5600	14.1089
1.3600	14.5563	1.5700	14.0903
1.3700	14.5299	1.5800	14.0721
1.3800	14.5040	1.5900	14.0542

$\frac{x_{\min}}{h}$	$\Delta\psi$ (deg)	$\frac{x_{\min}}{h}$	$\Delta\psi$ (deg)
1.6000	14.0366	1.8000	13.7386
1.6100	14.0193	1.8100	13.7260
1.6200	14.0022	1.8200	13.7136
1.6300	13.9855	1.8300	13.7015
1.6400	13.9690	1.8400	13.6895
1.6500	13.9528	1.8500	13.6777
1.6600	13.9368	1.8600	13.6660
1.6700	13.9212	1.8700	13.6546
1.6800	13.9057	1.8800	13.6433
1.6900	13.8905	1.8900	13.6322
1.7000	13.8756	1.9000	13.6212
1.7100	13.8609	1.9100	13.6104
1.7200	13.8464	1.9200	13.5998
1.7300	13.8322	1.9300	13.5894
1.7400	13.8182	1.9400	13.5790
1.7500	13.8044	1.9500	13.5689
1.7600	13.7908	1.9600	13.5588
1.7700	13.7774	1.9700	13.5490
1.7800	13.7643	1.9800	13.5392
1.7900	13.7513	1.9900	13.5297
		2.0000	13.5202

Table 6. Values of $\Delta\psi$ as a function of $\frac{x_{\min}}{h}$ for $\frac{\lambda}{L_y} = 0.5$ where $\Delta\psi$ is the 3-dB beamwidth of the vertical, far-field beam pattern, h is the altitude, $x_{\min}$ is the width of the one-sided blind zone, λ is the wavelength, and L_y is the aperture length in the Y direction.

$\frac{x_{\min}}{h}$	$\Delta\psi$ (deg)	$\frac{x_{\min}}{h}$	$\Delta\psi$ (deg)
0	56.1514	0.1700	47.4737
0.0100	55.5819	0.1800	47.0318
0.0200	55.0194	0.1900	46.5976
0.0300	54.4641	0.2000	46.1710
0.0400	53.9159	0.2100	45.7520
0.0500	53.3750	0.2200	45.3406
0.0600	52.8415	0.2300	44.9366
0.0700	52.3155	0.2400	44.5402
0.0800	51.7969	0.2500	44.1512
0.0900	51.2859	0.2600	43.7695
0.1000	50.7825	0.2700	43.3951
0.1100	50.2868	0.2800	43.0279
0.1200	49.7987	0.2900	42.6679
0.1300	49.3183	0.3000	42.3149
0.1400	48.8456	0.3100	41.9689
0.1500	48.3806	0.3200	41.6298
0.1600	47.9233	0.3300	41.2976

$\frac{x_{\min}}{h}$	$\Delta\psi$ (deg)	$\frac{x_{\min}}{h}$	$\Delta\psi$ (deg)
0.3400	40.9720	0.5500	35.5174
0.3500	40.6531	0.5600	35.3150
0.3600	40.3408	0.5700	35.1170
0.3700	40.0349	0.5800	34.9234
0.3800	39.7353	0.5900	34.7340
0.3900	39.4420	0.6000	34.5489
0.4000	39.1549	0.6100	34.3678
0.4100	38.8738	0.6200	34.1907
0.4200	38.5987	0.6300	34.0175
0.4300	38.3294	0.6400	33.8481
0.4400	38.0658	0.6500	33.6825
0.4500	37.8079	0.6600	33.5205
0.4600	37.5556	0.6700	33.3621
0.4700	37.3087	0.6800	33.2072
0.4800	37.0672	0.6900	33.0557
0.4900	36.8308	0.7000	32.9075
0.5000	36.5997	0.7100	32.7626
0.5100	36.3735	0.7200	32.6209
0.5200	36.1523	0.7300	32.4822
0.5300	35.9360	0.7400	32.3466
0.5400	35.7244	0.7500	32.2140

$\frac{x_{\min}}{h}$	$\Delta\psi$ (deg)	$\frac{x_{\min}}{h}$	$\Delta\psi$ (deg)
0.7600	32.0843	0.9700	29.9229
0.7700	31.9574	0.9800	29.8423
0.7800	31.8333	0.9900	29.7634
0.7900	31.7119	1.0000	29.6861
0.8000	31.5931	1.0100	29.6105
0.8100	31.4769	1.0200	29.5364
0.8200	31.3632	1.0300	29.4638
0.8300	31.2520	1.0400	29.3928
0.8400	31.1432	1.0500	29.3231
0.8500	31.0367	1.0600	29.2550
0.8600	30.9325	1.0700	29.1882
0.8700	30.8305	1.0800	29.1228
0.8800	30.7307	1.0900	29.0587
0.8900	30.6331	1.1000	28.9959
0.9000	30.5375	1.1100	28.9344
0.9100	30.4440	1.1200	28.8741
0.9200	30.3524	1.1300	28.8150
0.9300	30.2628	1.1400	28.7571
0.9400	30.1751	1.1500	28.7004
0.9500	30.0892	1.1600	28.6448
0.9600	30.0052	1.1700	28.5903

$\frac{x_{\min}}{h}$	$\Delta\psi$ (deg)	$\frac{x_{\min}}{h}$	$\Delta\psi$ (deg)
1.1800	28.5369	1.3900	27.6266
1.1900	28.4845	1.4000	27.5918
1.2000	28.4332	1.4100	27.5576
1.2100	28.3829	1.4200	27.5240
1.2200	28.3336	1.4300	27.4910
1.2300	28.2852	1.4400	27.4587
1.2400	28.2378	1.4500	27.4270
1.2500	28.1913	1.4600	27.3958
1.2600	28.1457	1.4700	27.3652
1.2700	28.1010	1.4800	27.3352
1.2800	28.0571	1.4900	27.3057
1.2900	28.0141	1.5000	27.2767
1.3000	27.9720	1.5100	27.2483
1.3100	27.9306	1.5200	27.2204
1.3200	27.8900	1.5300	27.1930
1.3300	27.8502	1.5400	27.1661
1.3400	27.8111	1.5500	27.1396
1.3500	27.7728	1.5600	27.1137
1.3600	27.7352	1.5700	27.0882
1.3700	27.6983	1.5800	27.0632
1.3800	27.6621	1.5900	27.0386

$\frac{x_{\min}}{h}$	$\Delta\psi$ (deg)	$\frac{x_{\min}}{h}$	$\Delta\psi$ (deg)
1.6000	27.0144	1.8000	26.6106
1.6100	26.9907	1.8100	26.5938
1.6200	26.9674	1.8200	26.5774
1.6300	26.9445	1.8300	26.5612
1.6400	26.9220	1.8400	26.5453
1.6500	26.8998	1.8500	26.5296
1.6600	26.8781	1.8600	26.5142
1.6700	26.8568	1.8700	26.4991
1.6800	26.8358	1.8800	26.4842
1.6900	26.8152	1.8900	26.4695
1.7000	26.7950	1.9000	26.4552
1.7100	26.7751	1.9100	26.4410
1.7200	26.7555	1.9200	26.4271
1.7300	26.7363	1.9300	26.4134
1.7400	26.7174	1.9400	26.3999
1.7500	26.6988	1.9500	26.3867
1.7600	26.6806	1.9600	26.3736
1.7700	26.6626	1.9700	26.3608
1.7800	26.6450	1.9800	26.3482
1.7900	26.6276	1.9900	26.3358
		2.0000	26.3236

Table 7. Values of $\Delta\psi$ as a function of $\frac{x_{\min}}{h}$ for $\frac{\lambda}{L_y} = 0.75$ where $\Delta\psi$ is the 3-dB beamwidth of the vertical, far-field beam pattern, h is the altitude, $x_{\min}$ is the width of the one-sided blind zone, λ is the wavelength, and L_y is the aperture length in the Y direction.

$\frac{x_{\min}}{h}$	$\Delta\psi$ (deg)	$\frac{x_{\min}}{h}$	$\Delta\psi$ (deg)
0	70.3971	0.1700	61.6070
0.0100	69.8272	0.1800	61.1523
0.0200	69.2635	0.1900	60.7046
0.0300	68.7060	0.2000	60.2640
0.0400	68.1550	0.2100	59.8305
0.0500	67.6105	0.2200	59.4041
0.0600	67.0726	0.2300	58.9847
0.0700	66.5413	0.2400	58.5723
0.0800	66.0167	0.2500	58.1669
0.0900	65.4989	0.2600	57.7685
0.1000	64.9880	0.2700	57.3770
0.1100	64.4840	0.2800	56.9924
0.1200	63.9869	0.2900	56.6146
0.1300	63.4969	0.3000	56.2436
0.1400	63.0138	0.3100	55.8793
0.1500	62.5378	0.3200	55.5216
0.1600	62.0689	0.3300	55.1706

$\frac{x_{\min}}{h}$	$\Delta\psi$ (deg)	$\frac{x_{\min}}{h}$	$\Delta\psi$ (deg)
0.3400	54.8261	0.5500	48.9663
0.3500	54.4880	0.5600	48.7456
0.3600	54.1564	0.5700	48.5297
0.3700	53.8311	0.5800	48.3182
0.3800	53.5121	0.5900	48.1113
0.3900	53.1992	0.6000	47.9087
0.4000	52.8924	0.6100	47.7105
0.4100	52.5917	0.6200	47.5165
0.4200	52.2969	0.6300	47.3266
0.4300	52.0079	0.6400	47.1408
0.4400	51.7248	0.6500	46.9589
0.4500	51.4473	0.6600	46.7810
0.4600	51.1754	0.6700	46.6069
0.4700	50.9090	0.6800	46.4365
0.4800	50.6481	0.6900	46.2698
0.4900	50.3925	0.7000	46.1067
0.5000	50.1422	0.7100	45.9471
0.5100	49.8970	0.7200	45.7910
0.5200	49.6569	0.7300	45.6382
0.5300	49.4218	0.7400	45.4888
0.5400	49.1916	0.7500	45.3426

$\frac{x_{min}}{h}$	$\Delta\psi$ (deg)	$\frac{x_{min}}{h}$	$\Delta\psi$ (deg)
0.7600	45.1995	0.9400	43.0947
0.7700	45.0596	0.9500	43.0003
0.7800	44.9226	0.9600	42.9080
0.7900	44.7887	0.9700	42.8176
0.8000	44.6576	0.9800	42.7292
0.8100	44.5294	0.9900	42.6427
0.8200	44.4040	1.0000	42.5581
0.8300	44.2812	1.0100	42.4753
0.8400	44.1612	1.0200	42.3942
0.8500	44.0437	1.0300	42.3149
0.8600	43.9288	1.0400	42.2373
0.8700	43.8164	1.0500	42.1614
0.8800	43.7064	1.0600	42.0871
0.8900	43.5988	1.0700	42.0144
0.9000	43.4935	1.0800	41.9432
0.9100	43.3905	1.0900	41.8736
0.9200	43.2898	1.1000	41.8054
0.9300	43.1912	1.1100	41.7387
		1.1200	41.6735

Table 8. Values of $\Delta\psi$ as a function of $\frac{x_{\min}}{h}$ for $\frac{\lambda}{L_y}=1$ where $\Delta\psi$ is the 3-dB beamwidth of the vertical, far-field beam pattern, h is the altitude, $x_{\min}$ is the width of the one-sided blind zone, λ is the wavelength, and L_y is the aperture length in the Y direction.

$\frac{x_{\min}}{h}$	$\Delta\psi$ (deg)	$\frac{x_{\min}}{h}$	$\Delta\psi$ (deg)
0	83.4540	0.1700	74.6211
0.0100	82.8840	0.1800	74.1615
0.0200	82.3198	0.1900	73.7087
0.0300	81.7616	0.2000	73.2629
0.0400	81.2095	0.2100	72.8239
0.0500	80.6636	0.2200	72.3919
0.0600	80.1239	0.2300	71.9667
0.0700	79.5906	0.2400	71.5485
0.0800	79.0638	0.2500	71.1370
0.0900	78.5434	0.2600	70.7325
0.1000	78.0296	0.2700	70.3347
0.1100	77.5224	0.2800	69.9437
0.1200	77.0219	0.2900	69.5594
0.1300	76.5281	0.3000	69.1819
0.1400	76.0411	0.3100	68.8110
0.1500	75.5610	0.3200	68.4467
0.1600	75.0876	0.3300	68.0890

$\frac{x_{\min}}{h}$	$\Delta\psi$ (deg)	$\frac{x_{\min}}{h}$	$\Delta\psi$ (deg)
0.3400	67.7378	0.4300	64.8602
0.3500	67.3931	0.4400	64.5706
0.3600	67.0547	0.4500	64.2869
0.3700	66.7227	0.4600	64.0089
0.3800	66.3970	0.4700	63.7364
0.3900	66.0775	0.4800	63.4696
0.4000	65.7641	0.4900	63.2081
0.4100	65.4568	0.5000	62.9521
0.4200	65.1555	0.5100	62.7014
		0.5200	62.4559

Table 9. Values of ψ' as a function of $\frac{x_{\min}}{h}$ for $\frac{\lambda}{L_y} = 0.25$ where ψ' is the beam-steer angle, h is the altitude, $x_{\min}$ is the width of the one-sided blind zone, λ is the wavelength, and L_y is the aperture length in the Y direction.

$\frac{x_{\min}}{h}$	ψ' (deg)	$\frac{x_{\min}}{h}$	ψ' (deg)
0	62.7792	0.1800	60.8601
0.0100	62.7729	0.1900	60.6538
0.0200	62.7541	0.2000	60.4390
0.0300	62.7229	0.2100	60.2159
0.0400	62.6792	0.2200	59.9850
0.0500	62.6233	0.2300	59.7466
0.0600	62.5551	0.2400	59.5009
0.0700	62.4750	0.2500	59.2484
0.0800	62.3829	0.2600	58.9895
0.0900	62.2792	0.2700	58.7243
0.1000	62.1639	0.2800	58.4533
0.1100	62.0375	0.2900	58.1768
0.1200	61.9000	0.3000	57.8951
0.1300	61.7518	0.3100	57.6085
0.1400	61.5932	0.3200	57.3173
0.1500	61.4244	0.3300	57.0219
0.1600	61.2457	0.3400	56.7225
0.1700	61.0575	0.3500	56.4194

$\frac{x_{\min}}{h}$	ψ' (deg)	$\frac{x_{\min}}{h}$	ψ' (deg)
0.3600	56.1129	0.5700	49.2906
0.3700	55.8032	0.5800	48.9626
0.3800	55.4906	0.5900	48.6354
0.3900	55.1754	0.6000	48.3090
0.4000	54.8579	0.6100	47.9836
0.4100	54.5381	0.6200	47.6593
0.4200	54.2165	0.6300	47.3361
0.4300	53.8931	0.6400	47.0141
0.4400	53.5683	0.6500	46.6934
0.4500	53.2421	0.6600	46.3740
0.4600	52.9149	0.6700	46.0561
0.4700	52.5867	0.6800	45.7397
0.4800	52.2578	0.6900	45.4248
0.4900	51.9284	0.7000	45.1115
0.5000	51.5985	0.7100	44.7999
0.5100	51.2684	0.7200	44.4900
0.5200	50.9382	0.7300	44.1818
0.5300	50.6081	0.7400	43.8754
0.5400	50.2781	0.7500	43.5708
0.5500	49.9485	0.7600	43.2680
0.5600	49.6192	0.7700	42.9672

$\frac{x_{\min}}{h}$	ψ' (deg)	$\frac{x_{\min}}{h}$	ψ' (deg)
0.7800	42.6682	0.9900	36.8628
0.7900	42.3713	1.0000	36.6094
0.8000	42.0762	1.0100	36.3581
0.8100	41.7832	1.0200	36.1089
0.8200	41.4922	1.0300	35.8617
0.8300	41.2032	1.0400	35.6166
0.8400	40.9162	1.0500	35.3736
0.8500	40.6313	1.0600	35.1326
0.8600	40.3485	1.0700	34.8936
0.8700	40.0678	1.0800	34.6567
0.8800	39.7891	1.0900	34.4218
0.8900	39.5125	1.1000	34.1889
0.9000	39.2381	1.1100	33.9580
0.9100	38.9657	1.1200	33.7290
0.9200	38.6955	1.1300	33.5021
0.9300	38.4273	1.1400	33.2770
0.9400	38.1613	1.1500	33.0540
0.9500	37.8974	1.1600	32.8328
0.9600	37.6356	1.1700	32.6136
0.9700	37.3759	1.1800	32.3963
0.9800	37.1183	1.1900	32.1808

$\frac{x_{\min}}{h}$	ψ' (deg)	$\frac{x_{\min}}{h}$	ψ' (deg)
1.2000	31.9672	1.4100	27.8883
1.2100	31.7555	1.4200	27.7121
1.2200	31.5457	1.4300	27.5374
1.2300	31.3376	1.4400	27.3643
1.2400	31.1314	1.4500	27.1926
1.2500	30.9270	1.4600	27.0224
1.2600	30.7243	1.4700	26.8537
1.2700	30.5234	1.4800	26.6864
1.2800	30.3243	1.4900	26.5206
1.2900	30.1269	1.5000	26.3562
1.3000	29.9313	1.5100	26.1932
1.3100	29.7373	1.5200	26.0316
1.3200	29.5450	1.5300	25.8714
1.3300	29.3545	1.5400	25.7125
1.3400	29.1655	1.5500	25.5550
1.3500	28.9782	1.5600	25.3988
1.3600	28.7926	1.5700	25.2439
1.3700	28.6086	1.5800	25.0904
1.3800	28.4261	1.5900	24.9381
1.3900	28.2453	1.6000	24.7872
1.4000	28.0660	1.6100	24.6375

$\frac{x_{\min}}{h}$	ψ' (deg)	$\frac{x_{\min}}{h}$	ψ' (deg)
1.6200	24.4890	1.8100	21.8908
1.6300	24.3418	1.8200	21.7649
1.6400	24.1959	1.8300	21.6400
1.6500	24.0511	1.8400	21.5161
1.6600	23.9076	1.8500	21.3932
1.6700	23.7652	1.8600	21.2713
1.6800	23.6241	1.8700	21.1504
1.6900	23.4841	1.8800	21.0304
1.7000	23.3452	1.8900	20.9113
1.7100	23.2075	1.9000	20.7932
1.7200	23.0709	1.9100	20.6760
1.7300	22.9355	1.9200	20.5598
1.7400	22.8011	1.9300	20.4444
1.7500	22.6679	1.9400	20.3300
1.7600	22.5357	1.9500	20.2164
1.7700	22.4046	1.9600	20.1037
1.7800	22.2746	1.9700	19.9919
1.7900	22.1456	1.9800	19.8809
1.8000	22.0177	1.9900	19.7708
		2.0000	19.6616

Table 10. Values of ψ' as a function of $\frac{x_{\min}}{h}$ for $\frac{\lambda}{L_y} = 0.5$ where ψ' is the beam-steer angle, h is the altitude, $x_{\min}$ is the width of the one-sided blind zone, λ is the wavelength, and L_y is the aperture length in the Y direction.

$\frac{x_{\min}}{h}$	ψ' (deg)	$\frac{x_{\min}}{h}$	ψ' (deg)
0	51.1234	0.1800	49.7013
0.0100	51.1189	0.1900	49.5458
0.0200	51.1052	0.2000	49.3832
0.0300	51.0824	0.2100	49.2139
0.0400	51.0506	0.2200	49.0380
0.0500	51.0097	0.2300	48.8557
0.0600	50.9599	0.2400	48.6673
0.0700	50.9011	0.2500	48.4729
0.0800	50.8336	0.2600	48.2728
0.0900	50.7574	0.2700	48.0672
0.1000	50.6726	0.2800	47.8563
0.1100	50.5793	0.2900	47.6403
0.1200	50.4777	0.3000	47.4194
0.1300	50.3679	0.3100	47.1939
0.1400	50.2500	0.3200	46.9639
0.1500	50.1242	0.3300	46.7297
0.1600	49.9907	0.3400	46.4915
0.1700	49.8497	0.3500	46.2495

$\frac{x_{min}}{h}$	ψ' (deg)	$\frac{x_{min}}{h}$	ψ' (deg)
0.3600	46.0039	0.5700	40.3366
0.3700	45.7549	0.5800	40.0556
0.3800	45.5027	0.5900	39.7746
0.3900	45.2475	0.6000	39.4937
0.4000	44.9895	0.6100	39.2129
0.4100	44.7288	0.6200	38.9324
0.4200	44.4657	0.6300	38.6522
0.4300	44.2003	0.6400	38.3725
0.4400	43.9329	0.6500	38.0933
0.4500	43.6635	0.6600	37.8147
0.4600	43.3923	0.6700	37.5367
0.4700	43.1196	0.6800	37.2595
0.4800	42.8454	0.6900	36.9831
0.4900	42.5700	0.7000	36.7076
0.5000	42.2934	0.7100	36.4330
0.5100	42.0158	0.7200	36.1594
0.5200	41.7373	0.7300	35.8869
0.5300	41.4582	0.7400	35.6154
0.5400	41.1784	0.7500	35.3451
0.5500	40.8981	0.7600	35.0760
0.5600	40.6175	0.7700	34.8081

$\frac{x_{min}}{h}$	ψ' (deg)	$\frac{x_{min}}{h}$	ψ' (deg)
0.7800	34.5415	0.9900	29.2848
0.7900	34.2761	1.0000	29.0522
0.8000	34.0122	1.0100	28.8213
0.8100	33.7496	1.0200	28.5921
0.8200	33.4884	1.0300	28.3646
0.8300	33.2286	1.0400	28.1388
0.8400	32.9703	1.0500	27.9146
0.8500	32.7136	1.0600	27.6921
0.8600	32.4583	1.0700	27.4713
0.8700	32.2045	1.0800	27.2522
0.8800	31.9523	1.0900	27.0347
0.8900	31.7017	1.1000	26.8190
0.9000	31.4527	1.1100	26.6048
0.9100	31.2052	1.1200	26.3924
0.9200	30.9594	1.1300	26.1815
0.9300	30.7152	1.1400	25.9724
0.9400	30.4727	1.1500	25.7649
0.9500	30.2318	1.1600	25.5590
0.9600	29.9925	1.1700	25.3547
0.9700	29.7550	1.1800	25.1520
0.9800	29.5190	1.1900	24.9510

$\frac{x_{min}}{h}$	ψ' (deg)	$\frac{x_{min}}{h}$	ψ' (deg)
1.2000	24.7516	1.4100	20.9160
1.2100	24.5537	1.4200	20.7492
1.2200	24.3574	1.4300	20.5838
1.2300	24.1628	1.4400	20.4198
1.2400	23.9696	1.4500	20.2571
1.2500	23.7781	1.4600	20.0957
1.2600	23.5880	1.4700	19.9356
1.2700	23.3996	1.4800	19.7768
1.2800	23.2126	1.4900	19.6193
1.2900	23.0272	1.5000	19.4631
1.3000	22.8432	1.5100	19.3082
1.3100	22.6608	1.5200	19.1545
1.3200	22.4798	1.5300	19.0020
1.3300	22.3003	1.5400	18.8508
1.3400	22.1223	1.5500	18.7008
1.3500	21.9457	1.5600	18.5521
1.3600	21.7705	1.5700	18.4045
1.3700	21.5968	1.5800	18.2581
1.3800	21.4245	1.5900	18.1128
1.3900	21.2536	1.6000	17.9688
1.4000	21.0841	1.6100	17.8259

$\frac{x_{\min}}{h}$	ψ' (deg)	$\frac{x_{\min}}{h}$	ψ' (deg)
1.6200	17.6841	1.8100	15.1940
1.6300	17.5435	1.8200	15.0730
1.6400	17.4040	1.8300	14.9528
1.6500	17.2656	1.8400	14.8336
1.6600	17.1283	1.8500	14.7153
1.6700	16.9921	1.8600	14.5980
1.6800	16.8570	1.8700	14.4815
1.6900	16.7229	1.8800	14.3659
1.7000	16.5899	1.8900	14.2512
1.7100	16.4580	1.9000	14.1373
1.7200	16.3271	1.9100	14.0243
1.7300	16.1972	1.9200	13.9122
1.7400	16.0683	1.9300	13.8009
1.7500	15.9405	1.9400	13.6904
1.7600	15.8136	1.9500	13.5808
1.7700	15.6878	1.9600	13.4720
1.7800	15.5629	1.9700	13.3640
1.7900	15.4390	1.9800	13.2568
1.8000	15.3160	1.9900	13.1504
		2.0000	13.0448

Table 11. Values of ψ' as a function of $\frac{x_{\min}}{h}$ for $\frac{\lambda}{L_y} = 0.75$ where ψ' is the beam-steer angle, h is the altitude, $x_{\min}$ is the width of the one-sided blind zone, λ is the wavelength, and L_y is the aperture length in the Y direction.

$\frac{x_{\min}}{h}$	ψ' (deg)	$\frac{x_{\min}}{h}$	ψ' (deg)
0	41.8936	0.1800	40.6875
0.0100	41.8898	0.1900	40.5548
0.0200	41.8783	0.2000	40.4159
0.0300	41.8590	0.2100	40.2710
0.0400	41.8322	0.2200	40.1203
0.0500	41.7977	0.2300	39.9639
0.0600	41.7556	0.2400	39.8021
0.0700	41.7060	0.2500	39.6348
0.0800	41.6490	0.2600	39.4625
0.0900	41.5845	0.2700	39.2851
0.1000	41.5128	0.2800	39.1028
0.1100	41.4338	0.2900	38.9159
0.1200	41.3477	0.3000	38.7245
0.1300	41.2546	0.3100	38.5288
0.1400	41.1545	0.3200	38.3289
0.1500	41.0476	0.3300	38.1250
0.1600	40.9341	0.3400	37.9173
0.1700	40.8140	0.3500	37.7059

$\frac{x_{min}}{h}$	ψ' (deg)	$\frac{x_{min}}{h}$	ψ' (deg)
0.3600	37.4910	0.5700	32.4475
0.3700	37.2729	0.5800	32.1936
0.3800	37.0516	0.5900	31.9392
0.3900	36.8273	0.6000	31.6846
0.4000	36.6001	0.6100	31.4298
0.4100	36.3703	0.6200	31.1749
0.4200	36.1380	0.6300	30.9201
0.4300	35.9033	0.6400	30.6653
0.4400	35.6664	0.6500	30.4106
0.4500	35.4274	0.6600	30.1562
0.4600	35.1865	0.6700	29.9021
0.4700	34.9439	0.6800	29.6484
0.4800	34.6995	0.6900	29.3952
0.4900	34.4537	0.7000	29.1424
0.5000	34.2065	0.7100	28.8902
0.5100	33.9580	0.7200	28.6387
0.5200	33.7084	0.7300	28.3878
0.5300	33.4578	0.7400	28.1377
0.5400	33.2063	0.7500	27.8883
0.5500	32.9540	0.7600	27.6398
0.5600	32.7011	0.7700	27.3922

$\frac{x_{\min}}{h}$	ψ' (deg)	$\frac{x_{\min}}{h}$	ψ' (deg)
0.7800	27.1455	0.9500	23.1257
0.7900	26.8998	0.9600	22.9008
0.8000	26.6551	0.9700	22.6774
0.8100	26.4114	0.9800	22.4553
0.8200	26.1688	0.9900	22.2347
0.8300	25.9274	1.0000	22.0155
0.8400	25.6870	1.0100	21.7977
0.8500	25.4478	1.0200	21.5813
0.8600	25.2099	1.0300	21.3664
0.8700	24.9731	1.0400	21.1529
0.8800	24.7376	1.0500	20.9409
0.8900	24.5034	1.0600	20.7304
0.9000	24.2704	1.0700	20.5212
0.9100	24.0388	1.0800	20.3136
0.9200	23.8085	1.0900	20.1074
0.9300	23.5795	1.1000	19.9026
0.9400	23.3519	1.1100	19.6993
		1.1200	19.4975

Table 12. Values of ψ' as a function of $\frac{x_{\min}}{h}$ for $\frac{\lambda}{L_y}=1$ where ψ' is the beam-steer angle, h is the altitude, $x_{\min}$ is the width of the one-sided blind zone, λ is the wavelength, and L_y is the aperture length in the Y direction.

$\frac{x_{\min}}{h}$	ψ' (deg)	$\frac{x_{\min}}{h}$	ψ' (deg)
0	33.8486	0.1800	32.7642
0.0100	33.8451	0.1900	32.6445
0.0200	33.8348	0.2000	32.5191
0.0300	33.8176	0.2100	32.3882
0.0400	33.7935	0.2200	32.2520
0.0500	33.7625	0.2300	32.1106
0.0600	33.7248	0.2400	31.9641
0.0700	33.6803	0.2500	31.8126
0.0800	33.6292	0.2600	31.6563
0.0900	33.5713	0.2700	31.4953
0.1000	33.5069	0.2800	31.3298
0.1100	33.4359	0.2900	31.1600
0.1200	33.3586	0.3000	30.9858
0.1300	33.2748	0.3100	30.8076
0.1400	33.1848	0.3200	30.6255
0.1500	33.0887	0.3300	30.4395
0.1600	32.9864	0.3400	30.2499
0.1700	32.8783	0.3500	30.0568

$\frac{x_{min}}{h}$	ψ' (deg)	$\frac{x_{min}}{h}$	ψ' (deg)
0.3600	29.8603	0.4400	28.1847
0.3700	29.6606	0.4500	27.9643
0.3800	29.4579	0.4600	27.7420
0.3900	29.2522	0.4700	27.5178
0.4000	29.0437	0.4800	27.2918
0.4100	28.8326	0.4900	27.0643
0.4200	28.6189	0.5000	26.8353
0.4300	28.4029	0.5100	26.6049
		0.5200	26.3732

Table 13. Values of $\Delta\theta$ as a function of $\frac{\Delta z_{\min}}{x_{\min}}$ where $\Delta\theta$ is the horizontal beamwidth $x_{\min}$ is the width of the one-sided blind zone, and $\Delta z_{\min}$ is the along-track resolution corresponding to $x_{\min}$.

$\frac{\Delta z_{\min}}{x_{\min}}$	$\Delta\theta$ (deg)	$\frac{\Delta z_{\min}}{x_{\min}}$	$\Delta\theta$ (deg)
0	0	0.1000	5.7248
0.0100	0.5730	0.1100	6.2962
0.0200	1.1459	0.1200	6.8673
0.0300	1.7187	0.1300	7.4380
0.0400	2.2915	0.1400	8.0083
0.0500	2.8642	0.1500	8.5783
0.0600	3.4367	0.1600	9.1478
0.0700	4.0091	0.1700	9.7169
0.0800	4.5812	0.1800	10.2855
0.0900	5.1531	0.1900	10.8536
		0.2000	11.4212

Table 14. Values of $\frac{\lambda}{L_z}$ as a function of $\frac{\Delta z_{\min}}{x_{\min}}$ where $\frac{\lambda}{L_z}$ is the ratio between the wavelength λ and L_z, which is the aperture length in the Z direction, $x_{\min}$ is the width of the one-sided blind zone, and $\Delta z_{\min}$ is the along-track resolution corresponding to $x_{\min}$.

$\frac{\Delta z_{\min}}{x_{\min}}$	$\frac{\lambda}{L_z}$	$\frac{\Delta z_{\min}}{x_{\min}}$	$\frac{\lambda}{L_z}$
0	0	0.1000	0.1127
0.0100	0.0113	0.1100	0.1240
0.0200	0.0226	0.1200	0.1352
0.0300	0.0339	0.1300	0.1464
0.0400	0.0451	0.1400	0.1576
0.0500	0.0564	0.1500	0.1688
0.0600	0.0677	0.1600	0.1800
0.0700	0.0790	0.1700	0.1912
0.0800	0.0902	0.1800	0.2023
0.0900	0.1015	0.1900	0.2135
		0.2000	0.2246

THIS PAGE INTENTIONALLY LEFT BLANK

LIST OF REFERENCES

[1] M. L. Somers and A. R. Stubbs, “Sidescan Sonar,” *IEE Proceedings*, vol. 131(F), pp. 243-256, 1984.

[2] J. M. Glynn and M. Buffman, “A Side Scan Sonar for Autonomous Underwater Vehicles*,” Proceedings of the 1996 Symposium on Autonomous Underwater Vehicles Technology*, pp. 154-159, June 1996.

[3] J. F. Wade, “Navy Tactics, Doctrine, and Training Requirements for Littoral Warfare,” Master’s Thesis, Naval Postgraduate School, Monterey, California, 1996.

[4] AUV Laboratory at MIT Sea Grant web site, http://auvlab.mit.edu/, last accessed July 2006.

[5] Stealth? The Hidden Pillar Organic Mine Countermeasures? Signature Control for a Force Protection web site, http://www.globalsecurity.org/military/library/report/2002/mil-02-04-wavelengths01.htm, last accessed July 2006.

[6] L. J. Ziomek, “Side-Looking Sonar (SLS),” Course Notes, EC4450 Sonar Systems Engineering, Naval Postgraduate School, Monterey, California, 2006.

[7] M. P. Bruce, “A Processing Requirement and Resolution Capability Comparison of Side-Scan and Synthetic-Aperture Sonars,” *IEEE Oceanic Engineering*, vol. 17, Issue 1, pp. 106-117, January 1992.

[8] K. Tomiyasu, “Tutorial Review of Synthetic-Aperture Radar (SAR) with Applications to Imaging the Ocean Surface,” *Proc. IEEE*, vol. 66, pp. 563-583, November 1978.

[9] L. J. Ziomek, *Fundamentals of Acoustic Field Theory and Space-Time Signal Processing (First Edition)*, CRC Press, Boca Raton, FL, 1995, pp. 401-480.

[10] A. Malinverno, M. H. Edwards, and W. B. F Ryan, “Processing of SeaMARC Swath Sonar Data,” *IEEE Oceanic Engineering*, vol. 15, Issue 1, pp. 14-23, January 1990.

[11] Private communication with Michael R. Medeiros, NUWC, Newport, RI.

[12] L. J. Ziomek, *Fundamentals of Acoustic Field Theory and Space-Time Signal Processing (First Edition)*, CRC Press, Boca Raton, FL, 1995, pp. 561-564.

[13] L. E. Kinsler, A. R Frey, A. B. Coppens and J.V. Sanders, *Fundamentals of Acoustics (Fourth Edition)*, John Wiley&Sons, New York, 2000, pp. 448-449.

[14] L. E. Kinsler, A. R Frey, A. B. Coppens and J.V. Sanders, *Fundamentals of Acoustics (Fourth Edition)*, John Wiley&Sons, New York, 2000, pp. 188-189.

[15] L. E. Kinsler, A. R Frey, A. B. Coppens and J.V. Sanders, *Fundamentals of Acoustics (Fourth Edition)*, John Wiley&Sons, New York, 2000, pp. 436-437.

[16] H. M. Marsh and M. Schulkin, "Sound Absorption in Sea Water," *Journal of the Acoustical Society of America*, vol. 34, Issue 6, pp. 864-865, 1962.

[17] W. H. Thorp, "Analytic Description of the Low-frequency attenuation coefficient," *Journal of the Acoustical Society of America*, vol. 42, Issue 1, pp. 270, 1967.

[18] W. H. Thorp, "Attenuation of Low Frequency Sound in the Ocean," *Journal of Sound and Vibration*, vol. 26, Issue 4, pp. 576-578, 1973.

[19] M. Schulkin, H. M. Marsh, "Low Frequency Sound Absorption in the Ocean," *Journal of the Acoustical Society of America,* vol. 63, Issue 1, pp. 43-48, 1978.

[20] J. R. Lovett, " Geographic Variation of Low-frequency Sound Absorption in the Pacific Ocean," *Journal of the Acoustical Society of America,* vol. 65, pp. 253-254, 1979.

[21] R. E Francois and G. R. Garrison, "Sound Absorption Based on Ocean Measurements. Part II Boric Acid Contribution and Equation for Total Absorption," *Journal of the Acoustical Society of America,* vol. 72, pp. 1879-1890, 1982.

[22] R. H. Wallace, H. V. Hillery, G. R. Barnard, B. M. Marks and C. M. McKinney, "Experimental Investigation of Several Passive Sonar Targets," *Journal of the Acoustical Society of America,* vol. 57, pp. 862-869, 1975.

[23] A. D. Waite, *Sonar for Practising Engineers (Third Edition)*," John Wiley&Sons, New York, 2002, pp. 72-73.

[24] A. D. Waite, *Sonar for Practising Engineers (Third Edition)*," John Wiley&Sons, New York, 2002, pp. 32-33.

[25] M. T. Shaw and R. O. Nielsen, "Performance Verification Testing of a High-Resolution Side-Looking Sonar," *MTS/IEEE Oceans 2001, Conference and Exhibition*, vol. 3, pp. 1745-1749, November 2001.

[26] L. E. Kinsler, A. R Frey, A. B. Coppens and J.V. Sanders, *Fundamentals of Acoustics (Fourth Edition)*, John Wiley&Sons, New York, 2000, pp. 309-311.

THIS PAGE INTENTIONALLY LEFT BLANK

INITIAL DISTRIBUTION LIST

1. Defense Technical Information Center
   Ft. Belvoir, Virginia

2. Dudley Knox Library
   Naval Postgraduate School
   Monterey, California

3. Chairman, Code PH/Lj
   Department of Physics
   Naval Postgraduate School
   Monterey, California

4. Chairman, Code IS/Bo
   Department of Information Sciences
   Naval Postgraduate School
   Monterey, California

5. Professor Lawrence J. Ziomek EC/Zm
   Department of Electrical and Computer Engineering
   Naval Postgraduate School
   Monterey, California

6. Professor Bruce Denardo PH/De
   Department of Physics
   Naval Postgraduate School
   Monterey, California

7. Embassy of Greece
   Office of Naval Attaché
   Washington, DC

8. Konstantinos Tsaprazis
   Athens Greece